Aspects of Numerical Simulation of Circulation Control Airfoils

R. C. Swanson, C. L. Rumsey, S. G. Anders
NASA Langley Research Center
Hampton, VA

Abstract

The mass-averaged compressible Navier-Stokes equations are solved for circulation control airfoils. Numerical solutions are computed with a multigrid method that uses an implicit approximate factorization smoother. The effects of flow conditions (e.g., free-stream Mach number, angle of attack, momentum coefficient) and mesh on the prediction of circulation control airfoil flows are considered. In addition, the impact of turbulence modeling, including curvature effects and modifications to reduce eddy viscosity levels in the wall jet (i.e., Coanda flow), is discussed. Computed pressure distributions are compared with available experimental data.

Introduction

Conventional high-lift systems use slats and flaps to create the necessary airfoil camber to achieve the desired circulation, and thus lift. There is a weight penalty and increased maintenance associated with these systems. For a number of years [1] aerodynamicists have been seeking alternative high-lift systems that can reduce the weight and complexity of the conventional systems. One such system for circulation control (CC) involves the Coanda effect. By controlling a jet discharged from a slot on the upper surface of the airfoil, the trailing edge stagnation point is moved forward on the lower surface, and the leading edge stagnation point is moved rearward. In this way the effective camber of the airfoil can be increased, resulting in the augmentation of lift. Previously, the weight and operational requirements of such systems have been unacceptable. The potential benefits of these CC systems in terms of reduced take-off and landing speeds as well as increased maneuverability have encouraged aerodynamicists to reconsider such systems. Moreover, the benefits of using pulsed jets offer the genuine possibility of significantly mitigating the obstacles preventing the implementation of these CC systems [2].

Computational methods will play a vital role in designing effective CC configurations. Certainly, detailed experimental data, such as velocity profiles and Reynolds stresses, will be absolutely essential for validating these prediction tools. Due to the cost of flow control experiments, design and parametric studies will strongly depend on accurate and efficient prediction methods. These methods must have the potential to treat pulsating jets, even multiple jets, for a broad range of flow conditions (e.g., Mach number, Reynolds number, angle of attack). In general, the numerical methods must be extendable to time-dependent and three-dimensional flows.

A number of computational methods have been applied to CC airfoil flows. In 1985 Pulliam et al. [3] used ARC2D [4], an implicit Navier-Stokes solver, to compute solutions for two of the CC configurations tested by Abramson and Rogers [5]. A spiral grid that begins in the plenum and wraps around the airfoil several times was used for the computations. Turbulence modeling of the flow over the airfoil and Coanda surface was done by applying a modified form of the zero-equation model of Baldwin and Lomax [6]. A term was introduced in the model to account for streamline curvature effects. The modification includes a constant C_c. This constant was modified for each set of experimental conditions, and a set is defined by Coanda geometry, free-stream Mach number (M_∞), angle of attack (α), and a range of jet momentum coefficient C_μ. The C_c was adjusted so that the computed C_L matched the experimental value for one of the C_μ values. Then this C_c was used in computing all of the cases for the given set of conditions. Certainly, this approach is not satisfactory in general for modeling the turbulence. Nevertheless, Pulliam et al. were able to obtain good comparisons with experimental data for all cases considered. This work demonstrated that accurate Navier-Stokes simulation of CC airfoil flows is possible, and turbulence modeling is the key issue.

In 2002 Slomski et al. [7] considered the effects of turbulence modeling on the prediction of CC airfoil flows. Calculations were performed for the NCCR 1510-7067 airfoil, which is a cambered, 15 percent thick, CC airfoil with a jet slot located on the upper surface just upstream of the trailing edge. The airfoil was at zero degree angle of attack. Two variations of a two-equation transport model ($k-\epsilon$ model) and a Reynolds stress model were used for modeling turbulence. Predictions of surface pressures with the two-equation model compared favorably with the experimental data at low blowing rates. At high rates of blowing only the Reynolds stress model provided predictions that compare well with the data. A principal conclusion of Slomski et al. is that non-isotropic turbulence models are probably required for the simulation of circulation control airfoils or lifting surfaces.

Recently, Paterson and Baker [8] used an incompressible Navier-Stokes code to calculate the flow over the same CC airfoil considered by Slomski et al. They obtained solutions for the high blowing rate case that Slomski et al. computed and a case with the same free-stream conditions but an α of -8 degrees. The shear stress transport (SST) model of Menter [16] was used to model turbulence. Using this isotropic turbulence model their predicted surface pressure distributions compared favorably with experiment, even though an incompressible simulation was performed. However, it should be pointed out that the variation in the ratio of the jet density to the free-stream density for the α of zero degree case can vary roughly from 0.8 to 1.2. Thus, there are compressibility effects, and these may be quite important when attempting to predict the characteristics of the jet.

In the current work various aspects of simulating CC airfoil flows are examined. These aspects include the following: 1) flow conditions, 2) grid density, 3) turbulence modeling. The primary purpose of this paper is to provide some guidelines for accurate solutions and to delineate improvements needed in numerical techniques to reliably predict CC flows, eventually including pulsed jets. The compressible, mass-averaged Navier-Stokes equations are solved with a finite-volume approach for discretization. The equations are solved on a multi-block, patched grid, and a multigrid method with an implicit approximate factorization scheme is used to integrate the equations. Numerical solutions are obtained for flow over the CC geometry tested by Abramson and Rogers [5]. Several turbulence models are considered, including models based on one transport equation and two transport equations. A two-equation explicit algebraic Reynolds stress model is also considered. The influence of turbulence modeling is revealed by comparing computed and experimental pressure

Case	M_∞	Re_c	α (deg.)	C_μ
302	0.6	5.2×10^6	0	0.0032
283	0.12	5.45×10^5	0	0.2090
321	0.12	5.45×10^5	-8	0.1840

Table 1: Flow conditions for CC airfoil flows.

distributions, as well as Coanda jet streamlines.

The initial sections of the paper concern the CC airfoil geometry and flow conditions, description of grids, numerical method, and boundary conditions. This is followed by a section on turbulence modeling, where particular emphasis is given to modifications introduced into the models, and also, implementation details of the models that can significantly affect their performance. In the final sections the numerical results are discussed and concluding remarks are given.

Geometry and Grid

The CC geometry for the 2004 Circulation Control Workshop held at NASA Langley Research Center is the CC elliptical airfoil, which is designated NCCR 1510-7067N. This airfoil has a chord of 8 inches, thickness ratio of 15 percent, and a camber ratio of 1 percent. The jet slot height-to-chord ratio is 0.0030, which corresponds to a slot height of 0.024 inches.

Previously, we performed calculations for the CC airfoil which was tested by Abramson and Rogers [5]. This airfoil, which is designated as 103RE, has a chord of 18 inches, thickness ratio of 16 percent, and a camber ratio of 1 percent. The jet slot height-to-chord ratio is 0.0021, which corresponds to a slot height of 0.0378 inches. This CC airfoil is compared with the NCCR 1510-7067N airfoil in Fig. 1. The most significant differences between the two configurations are the size of the plenum and the jet slot height. Since the computational grid for the 103RE airfoil was available, and this geometry is quite similar to the one of the workshop, we elected to use the 103RE airfoil in simulating the workshop cases. In order to compute solutions for the workshop cases, we applied the free-stream conditions for these cases and matched the corresponding jet momentum coefficients.

In this paper we consider CC airfoil flows for high and low free-stream Mach numbers. The designated case numbers, which are associated with the experiments, and the flow conditions are given in Table 1. The definition of C_μ is given in a later section. For Case 302 the testing was done by Abramson and Rogers [5], and for Cases 283 and 321 the experimental data was obtained by Abramson [9]. Surface pressure distributions are available from the experiments. There are no velocity profiles or Reynolds stresses to allow a detailed assessment of turbulence models. Nevertheless, pressure data provides an opportunity for initial evaluation of the models. The experimental lift coefficients were determined by integrating the surface pressures, and the drag coefficients were computed from wake survey data using a momentum deficit method. Thus, the drag values include the propulsion effects due to the Coanda jet. Several sources of error in the experimental data were reported by Abramson [9]. While the experiments were generally two dimensional, there were three-demensional effects produced at the high blowing rates. Also, there

were changes in the slot height caused by the higher pressures required for the high blowing rates. We have not accounted for these effects on the experimental data.

For the numerical computations the domain surrounding the CC airfoil extended 20 chords away from the airfoil. This domain was partitioned with three blocks. At the interface boundary on the lower airfoil surface the grid is patched, as seen in Fig. 2, which displays the near field of a medium resolution grid. This grid includes 235 grid points around the airfoil and 49 points in the normal direction over the forward part of the airfoil. Over the aft part of the airfoil there are 101 points in the normal direction, and this number includes the points in the plenum for the jet. For the fine grid the number of cells in the medium grid is doubled in each coordinate direction, resulting in 70,563 points. The clustering of the grid at the airfoil leading edge and jet slot is clearly seen in Fig. 3 and Fig. 4. In the normal direction the grid is clustered at the surface so that the normalized coordinate y^+ is less than one for the first point off the wall. The quantity y^+ is defined by $y\sqrt{\tau_w/\rho}/\nu$, where τ_w is the shear stress at the wall, ρ is density, and ν is the kinematic viscosity.

Numerical Method

Numerical solutions were computed with CFL3D, a multi-zone mass-averaged Navier-Stokes code developed at NASA Langley [10]. It solves the thin-layer form of the Navier-Stokes equations in each of the (selected) coordinate directions. It can use one-to-one, patched, or overset grids, and employs local time step scaling, grid sequencing, and multigrid to accelerate convergence to steady state. In time-accurate mode, CFL3D has the option to employ dual-time stepping with subiterations and multigrid, and it achieves second-order temporal accuracy.

The code CFL3D is based on a finite-volume method. The convective terms are approximated with third-order upwind-biased spatial differencing, and both the pressure and viscous terms are discretized with second-order central differencing. The discrete scheme is globally second-order spatially accurate. The flux difference-splitting (FDS) method of Roe is employed to obtain fluxes at the cell faces. Advancement in time is accomplished with an implicit approximate factorization method (number of factors determined by number of dimensions).

In CFL3D, the turbulence models are implemented uncoupled from the mean-flow equations. The turbulent transport equations are solved using a two-factor implicit approximate factorization approach. The advection terms are discretized with first-order upwind differencing. The production source term is treated explicitly, while the advection, destruction, and diffusion terms are treated implicitly. For the explicit algebraic Reynolds stress (EASM-ko) model, the nonlinear terms are added to the Navier-Stokes equations explicitly.

Boundary and Initial Conditions

Boundary conditions are required at the inflow (internal and external), outflow, and solid surface boundaries. For numerical computations the physical boundary conditions must be supplemented with numerical boundary conditions, which generally involve extrapolation of flow quantities or combinations of them (e.g., Riemann invariants) from the interior of the domain. Discussion of the numerical boundary conditions is given in the user's manual for CFL3D [10]. At the far-field inflow boundary a Riemann invariant, entropy, and flow inclination angle are specified. A Riemann

invariant is specified at the far-field outflow boundary. For the plenum the mass flow rate and flow inclination angle are prescribed. If the mass flow rate is not known from the experiment, it is determined with an iterative process where it is changed until the experimental C_μ at the jet exit is matched. At the surface boundaries the no-slip and adiabatic wall conditions are specified. Boundary conditions for the various turbulence models considered herein are given in [10]. The initial solution is defined by the free-stream conditions.

Turbulence Modeling

Several turbulence models for computing CC airfoil flows are considered. The three principal models are the one-equation Spalart-Allmaras (SA) model [11], the Spalart-Allmaras rotation/curvature (SARC) model [12, 13], and the two-equation shear-stress transport (SST) model of Menter [14, 15, 16]. In addition, the zero-equation Baldwin-Lomax (BL) model [6] and the explicit algebraic stress (EASM) model in k-ω form (EASM-ko) [17] are used. The three primary models and the BL model are all linear eddy-viscosity models that make use of the Boussinesq eddy-viscosity hypothesis, whereas the EASM-ko model is a nonlinear model. The equations describing these four models can be found in their respective references. However, there are certain details concerning the implementation of the SARC and SST models that should be given here in order to facilitate the discussion of the numerical results.

The SA model can be written in general form as

$$\frac{D\tilde{\nu}}{Dt} = \mathcal{P} + \mathcal{D}_{diff} + \mathcal{D}_{diss} \tag{1}$$

where $\tilde{\nu} \sim \nu_t$, and $\mathcal{P}$, $\mathcal{D}_{diff}$, and $\mathcal{D}_{diss}$ are the contributions associated with turbulence due to production, diffusion, and dissipation, respectively. The production term is given by

$$\mathcal{P} = c_{b1}[1 - f_{t2}]W\tilde{\nu}. \tag{2}$$

In the SARC model $\mathcal{P}$ is replaced by

$$\mathcal{P}' = c_{b1}[f_{r1} - f_{t2}]W\tilde{\nu}, \tag{3}$$

$$f_{r1} = (1 + c_{r1})\frac{2r^*}{(1 + r^*)}\left[1 - c_{r3}\tan^{-1}(c_{r2}\tilde{r})\right] - c_{r1}, \tag{4}$$

where the function r^* is the ratio of scalar measure of strain rate to the scalar measure of rotation, the function $\tilde{r}$ depends on the Lagrangian derivative of the strain-rate tensor principal axes angle (see [13] for details), and $c_{r1} = 1$, $c_{r2} = 12$, and $c_{r3} = 0.6 - 1.0$. As c_{r3} is increased, the turbulence production will decrease near convex surfaces. Later, we will exploit this behavior to reduce the production of turbulence in the Coanda flow.

The production term $\mathcal{P}_k$ in the turbulent kinetic energy equation of the Menter SST model can be written as

$$\mathcal{P}_k = \tau_{ij}\frac{\partial u_i}{\partial x_j}, \tag{5}$$

where the stress tensor τ_{ij} is defined as

$$\tau_{ij} = \mu_t\left(\frac{\partial u_i}{\partial x_j} + \frac{\partial u_j}{\partial x_i} - \frac{2}{3}\frac{\partial u_k}{\partial x_k}\delta_{ij}\right) - \frac{2}{3}\rho k\delta_{ij}, \tag{6}$$

and μ_t is the turbulent viscosity, the partial derivatives are strain rates, and k is the turbulent kinetic energy. The production term $\mathcal{P}_\omega$ in the ω equation of the SST model is proportional to $\mathcal{P}_k$. Generally, in the computations with the SST model, the incompressible assumption is imposed, and the turbulent kinetic energy contribution is neglected. Thus,

$$\mathcal{P}_k = \mu_t(\frac{\partial u_i}{\partial x_j} + \frac{\partial u_j}{\partial x_i})\frac{\partial u_i}{\partial x_j} = 2\mu_t S_{ij} S_{ij}, \tag{7}$$

where S_{ij} is the strain-rate tensor, and $S_{ij}S_{ij}$ represents the double dot product of two tensors. When the strain-rate tensor is used for $\mathcal{P}_k$, the SST model will be designated SST(1994). In some versions of the SST model, also referenced as SST(baseline) model herein, the vorticity is substituted for the strain rate (see Menter [14]). In this case the production term is written as

$$\mathcal{P}_k = 2\mu_t W_{ij} W_{ij} = \mu_t |\Omega|^2, \tag{8}$$

where $|\Omega|$ is the magnitude of the vorticity vector. The vorticity is used with the default SST model in the CFL3D code. Certainly, one would not expect much difference in boundary-layer type flows between using strain rate or vorticity in the production terms.

The eddy viscosity determined with the SST model is defined as

$$\nu_t = \frac{a_1 k}{max(a_1\omega; \Omega F_2)}, \tag{9}$$

where a_1 is a constant, ω is equal to the ratio of the turbulent dissipation rate to the turbulent kinetic energy, $\Omega = \sqrt{2W_{ij}W_{ij}}$, and F_2 is a blending function. In the recent paper by Menter et al. [18], the Ω in Eq. 8 is replaced by $S = \sqrt{2S_{ij}S_{ij}}$. In the default SST model in CFL3D the Ω is used. Attempts to use S instead of Ω in this work resulted in nonphysical behavior of the solution for high blowing rates.

Jet Momentum Coefficient

A frequently used parameter in circulation control is the jet momentum coefficient, which is defined as

$$C_\mu = \frac{\dot{m}_j V_j}{\frac{1}{2}\rho_\infty {V_\infty}^2 A} = \frac{\rho_j {V_j}^2 hb}{\frac{1}{2}\rho_\infty {V_\infty}^2 cb},$$

where the quantity $\dot{m}$ is mass flow rate, V is velocity, ρ is density, and the subscripts j and ∞ refer to jet and free-stream conditions, respectively. The quantities A, b and c are the wing planform area, span, and chord, respectively, and h is the jet slot height. Therefore,

$$C_\mu \sim \frac{1}{M_\infty^2}. \tag{10}$$

Assume the same jet conditions. Then (roughly) for $M_\infty = 0.12$ and $M_\infty = 0.6$

$$(C_\mu)_{M=0.6} \approx \frac{(C_\mu)_{M=0.12}}{25}$$

So, at higher Mach numbers, small values of C_μ can be, in some sense, equivalent to higher values of C_μ at lower Mach numbers. One must keep this in mind when interpreting C_μ as M_∞ increases.

Numerical Results

The computational method described in previous sections was applied first to the high Mach number flow over the CC airfoil 103RE, which is Case 302 in Table 1. Calculations were performed on the medium grid. A comparison of the surface pressure distributions computed with the BL, SA, SST(baseline), and the anisotropic EASM-ko models is shown in Fig. 5. There is a significant discrepancy between the calculated and experimental [5] pressures for all of the turbulence models. Moreover, the predicted lift coefficient (C_L) is about two times the experimental C_L of 0.191 for all models. Since all of the models predict separation on the Coanda surface downstream of the location indicated by the experiment, this means that each model is producing near wall eddy viscosity values on the Coanda surface that are too high. Thus, too much high momentum fluid is being transferred to the inner part of the shear layer. For the transport equation models this indicates that the production of turbulent kinetic energy (TKE) is too high. To determine the effect of reducing the TKE, we decided to use the curvature correction term in the SARC model as a vehicle for TKE reduction.

As discussed in the turbulence modeling section, the c_{r3} parameter in the curvature correction term of the SARC model can provide a means to reduce the TKE in the Coanda flow. In Fig. 6 the influence of this parameter on the computed variations in pressure is displayed. With $c_{r3} = 9.6$ there is good agreement with the experimental data. The calculated C_L is 0.177, which underpredicts the experimental value by approximately 7 percent. Figure 7 shows the effect of c_{r3} on the variation in the turbulent viscosity μ_t in the direction normal to the airfoil trailing edge (x-axis). The dashed line represents $c_{r3} = 0.6$, which is the standard value for curvature correction, and the thin solid line refers to $c_{r3} = 9.6$. With $c_{r3} = 9.6$ there is a maximum reduction factor in μ_t of about 3 in the shear layer near the surface.

Figures 8 - 10 reveal the basic physics of the flow. In Fig. 8 the initial entrainment of the upper surface flow produced by the jet flow is discernible. A shear layer develops due to the entrainment. The early and subsequent development of the shear layer is evident. The Mach contours (with an interval of 0.04) in Fig. 9 indicate the rather thick boundary layers that develop on the upper and lower surfaces of the airfoil. They also suggest the separation of the Coanda jet. In Fig. 10 the separation of the jet flow is delineated by the streamline pattern. The flow over the blunt trailing edge separates later, but still upstream of the trailing edge, with the jet than without the jet. This delay in separation results in one of the vortices normally appearing in the blunt trailing edge region being eliminated.

In the subsequent discussion we consider results for the same airfoil at low Mach number, with several different blowing coefficients. For the first group of cases solutions were obtained on the medium grid with the SA, SARC($c_{r3} = 9.6$), and SST(baseline) turbulence models for various C_μ values. Comparisons are made in Fig. 11 between the computed and experimental [9] pressure distributions for $C_\mu = 0.026$. With the SA model there is significant disagreement with the data on the lower and upper surfaces of the airfoil. There is improvement in the agreement with the SST(baseline) model. The solution with the SARC model and $c_{r3} = 9.6$ exhibits relatively good agreement with the data. Figure 12 shows the Coanda jet streamlines for the SARC($c_{r3} = 9.6$) model. The vortex pair usually occurring behind the blunt trailing edge is conspicuously absent.

To provide some indication of convergence behavior of the computations, the variation with multigrid cycles in the L_2 norm of the residual (for density equation) is presented in Fig. 13. Roughly 7500 cycles are required to reduce the residual four orders of magnitude. A major contribution

to this slow convergence is the slowly converging plenum solution, which is a consequence of the very low-speed flow in the plenum. The implementation of low-speed preconditioning [19, 20, 21], especially in the plenum, should result in a significant acceleration of convergence. Recently, we tested preconditioning for this particular case. Without any attempt to optimize the performance of the preconditioning, the number of cycles required to attain the same level of convergence obtained previously was reduced by a factor of two. It should be mentioned that the need for preconditioning to achieve accurate solutions in very low-speed regions has been demonstrated [20].

In Fig. 14 the computed pressures when $C_\mu = 0.093$ are shown. Generally, the trends described for $C_\mu = 0.026$ are exhibited here as well. For this case solutions with both the SA and SST(baseline) models indicate jet wraparound (i.e., Coanda jet moves onto the lower surface of the airfoil), as supported by the reduced pressures on the airfoil lower surface. These reduced pressures are associated with the occurrence of recirculation. The jet wraparound with the SA model is seen in Fig. 15. With the SARC($c_{r3} = 9.6$) model there is generally good agreement with the data. However, a thin separation region (about 0.01 chord in maximum thickness) occurs just downstream of the airfoil leading edge. This separation results in a barely discernible plateauing effect on the calculated pressures, which is not consistent with the experimental data. Figure 16 shows the jet streamlines for the SARC model and the stronger jet penetration (relative to that in Fig. 12) into the flow field due to the increased C_μ.

The final two cases, which are Case 283 and Case 321, are those considered in the 2004 Circulation Control Workshop held at NASA Langley Research Center. Flow conditions for these cases are given in Table 1. For Case 283, where $C_\mu = 0.209$, the computed pressure distributions on the medium grid are compared with the experimental data in Fig. 17. There is considerable reduction in the computed lower surface pressures with the SA and SST(baseline) models relative to the experimental values. Such behavior indicates extensive flow separation on the lower surface with these models. In fact, the Coanda jet in these cases wraps around the trailing edge and moves even further upstream than shown in Fig. 15, a completely unphysical situation. The result with the SARC($c_{r3} = 9.6$) model exhibits fairly good agreement with the data on the lower airfoil surface, but it shows a plateau behavior over more than 50 percent of the airfoil on the upper surface. Thus, there is a large separation bubble on the upper surface. Numerical tests confirmed that this is a consequence of the large c_{r3} value being used for the SARC model in the airfoil leading edge region. By simply setting $c_{r3} = 9.6$ on the Coanda surface and taking it to be zero elsewhere, relatively good agreement with the data is again obtained for the SARC($c_{r3} = 0 - 9.6$) model.

The jet streamlines for the SARC($c_{r3} = 0 - 9.6$) model on the fine grid are presented in Fig. 18. In the Mach contours of Figs. 19 and 20 the rearward movement of the leading edge stagnation point, due to the Coanda effect, and the acceleration of the Coanda flow are seen. Details of the Mach contours at the jet exit, along with the corresponding fine grid, are displayed in Figs. 21 and 22. The jet flow is accelerated to a Mach number exceeding 0.9, indicating the compressible character of the jet.

There is only a small effect of mesh refinement on the solution calculated with the SARC($c_{r3} = 0 - 9.6$) model. Although not shown, the fine grid solution for the surface pressures nearly coincides with the medium grid solution. In addition, the velocity fields for the two grids are quite similar, as evident in velocity profiles shown in Figs. 23 and 24. Table 2 compares the predicted lift coefficient and drag coefficient (C_D) with the experimental values. In addition, the change in aerodynamic coefficients with further increases in C_μ are indicated. It must be kept in mind that there is some effect, although it may be small, on these low-speed predictions due to the differences between the

Case	C_μ	Grid	$(C_L)_{\exp}$	C_L	$(C_D)_{\exp}$	C_D
283	0.209	med.	4.20	3.26	-0.050	0.1140
283	0.209	fine	4.20	3.15	-0.050	0.1090
	0.281	med.		3.62	-0.050	0.1560
	0.342	med.		4.05	-0.050	0.2100
321	0.184	med.	3.10	2.17	-0.080	0.0957
321	0.184	fine	3.10	2.03	-0.080	0.0922

Table 2: Comparison of computed, with SARC($c_{r3} = 0 - 9.6$) model, and experimental lift and drag coefficients for circulation control airfoil.

103RE and the NCCR geometries.

As indicated in the section on turbulence modeling, Menter [15] has considered two ways to define the turbulence production terms of the SST model. For all of the previous SST(baseline) results that we have shown the production term was computed with vorticity (see Eq. 8). Now, we consider the impact of evaluating the production term using the principal strain-rate tensor (Eq. 7), as presented by Menter in his 1994 paper [16]. As mentioned earlier, we refer to this form of the SST model as SST(1994).

A comparison of the pressure distributions calculated with the SST(baseline) and SST(1994) turbulence models is shown in Fig. 25 for Case 283. Both medium and fine grid results are given. There is relatively good agreement with the data when applying the SST(1994) model, whereas the SST(baseline) results exhibit poor agreement. Thus, although use of Eq. 8 for the SST model has proven to be satisfactory for many aerodynamic flows of interest, it does not appear to be appropriate for the Coanda jet flows being considered here.

There is greater sensitivity to mesh refinement with the SST(1994) model than that experienced with the SARC($c_{r3} = 0 - 9.6$) model. The effect of mesh refinement on the Coanda surface skin-friction distributions calculated with these two models is shown in Fig. 26. Comparing Figs. 18 and 27, the jet streamlines with the SST(1994) model exhibit less spreading than those with the SARC($c_{r3} = 0-9.6$) model. Mesh refinement effect on the predicted C_L and C_D with the SST(1994) model is given in Table 3. While there is a reduction in C_L as the mesh is refined, as shown in Fig. 28, the lift augmentation (slope of C_L versus C_μ) appears to remain about the same for SST(1994) with mesh refinement. In the C_L predictions with both models shown in Fig. 28 there is a monotonic increase in C_L with increasing C_μ. The two-equation $k - \epsilon$ models considered by Slomski et al. [7] result in a nonphysical decrease in C_L beyond a C_μ of 0.093 (i.e., jet wraparound predicted).

For the second case (Case 321, angle of attack of -8 degrees) of the workshop, computed surface pressures for the medium and fine grids are presented in Figs. 29 and 30. Results with both the SST(1994) and SARC($c_{r3} = 0 - 9.6$) models compare favorably with the experimental data. Nevertheless, the experimental C_L is underpredicted by more than 22 percent (see Tables 2 and 3). Paterson and Baker [8] obtained the same value for the C_L of this case using the SST(1994) model and performing an incompressible simulation for flow over the NCCR-1510-7067N geometry. With the SARC($cr3 = 0 - 9.6$) model there is again greater spreading of the jet than with SST(1994), as

Case	C_μ	Grid	$(C_L)_{\exp}$	C_L	$(C_D)_{\exp}$	C_D
283	0.209	med.	4.20	4.19	-0.050	0.0966
283	0.209	fine	4.20	3.88	-0.050	0.0746
321	0.184	med.	3.10	2.96	-0.080	0.0655
321	0.184	fine	3.10	2.41	-0.080	0.0559

Table 3: Comparison of computed, with SST(1994) model, and experimental lift and drag coefficients for circulation control airfoil.

revealed by comparing Figs. 31 and 32 depicting the jet streamlines and Mach contours. There is an extremely small recirculation region, which occurs only for the SST(1994) model, on the lower surface that centers near the 0.92 chord location, but it is not visible in Fig. 32.

Concluding Remarks

A computational method (CFL3D) has been applied to both low and high subsonic Mach number CC airfoil flows. Several turbulence models have been investigated. These models include the one-equation SA model with curvature correction (SARC) and two variations of the two-equation shear stress transport (SST) model of Menter. For the high subsonic Mach number CC flow (Case 302), all models have predicted separation downstream of the experimental location, resulting in a significant overprediction of lift. In other words, all of the models have produced near wall eddy viscosity levels that are too high in the Coanda flow. A parameter (c_{r3}) in the curvature correction term of the SARC model has been used as a vehicle to explore the effect of reducing the turbulent kinetic energy in the Coanda flow. In so doing, relatively good agreement with the experimental pressure distribution of Case 302 has been obtained.

In the simulation of low Mach number CC airfoil flows a set of calculations has been performed for a range of values of C_μ. The two cases of the 2004 Circulation Control Workshop have also been considered. Relatively good agreement with experimental pressure data has been obtained when modeling turbulence with the SARC($c_{r3} = 0 - 9.6$) and the SST(1994) models. The SST(1994) model uses principal strain rate for the shear stress in the modeling of the turbulence production. The SST(baseline) model, which uses vorticity in the turbulence production term, has not been satisfactory when computing Coanda jet flows. An indication of the effects of grid refinement on the results computed with the turbulence models has been given. The SST(1994) model has shown greater sensitivity to mesh refinement than the SARC(0 - 9.6) model. Lift and drag coefficients have also been determined in the calculations.

Clearly, turbulence modeling is the major component in determining the success of a computational method for predicting CC airfoil flows. Further investigation of models is essential to achieving a reliable prediction technique that can be used for a broad range of flow conditions.

In addition, improvements in computational efficiency must also be considered quite important if the prediction method is to be applied on a routine basis with a high degree of reliability. Some rather straightforward numerical algorithm features such as low-speed preconditioning should be included in the method. Potential benefits of this preconditioning have been indicated in this paper.

Another possible improvement in computational performance can be achieved by full coupling of the fluid dynamic and turbulence transport equations, which is not done currently with the CFL3D code. These and other improvements in computational efficiency are especially important as the heiarchy (i.e., complexity) of the turbulence modeling is increased. For example, if a full Reynolds stress model is used instead of a two-equation model, such as SST(1994), one must anticipate that there will be a reduction in computing efficiency, due to a lower degree of numerical compatibility of the more complex model. In the case of steady flows, numerical compatibility can be defined as a measure of the effect on solution convergence of the complete system of flow equations due to turbulence modeling.

References

[1] Englar, R. J, and Williams, R. M., "Test Techniques for High Lift Two-Dimensional Airfoils with Boundary Layer and Circulation Control for Application to Rotary Wing Aircraft," *Canadian Aeronautics and Space J.*, vol. 19, No. 3, pp. 93–108, 1973.

[2] Jones, G. S., Viken, S. A, Washburn, A. E., Jenkins, L. N., Cagle, C. M., "An Active Flow Circulation Controlled Flap Concept for General Aviation Aircraft Applications," *AIAA Paper* 03-3157, 2003.

[3] Pulliam, T. H., Jespersen, D. C, Barth, T. J., "Navier-Stokes Computations for Circulation Control Airfoils," *AIAA Paper* 85-1587, 1985.

[4] Pulliam, T. H., "Euler and Thin Layer Navier-Stokes Codes: ARC2D, ARC3D," *Notes for Computational Fluid Dynamics User's Workshop*, The University of Tennessee Space Institute, Tullahoma, Tennessee, March 12–16, 1984.

[5] Abramson, J., and Rogers, E., "High-Speed Characteristics of Circulation Control Airfoils," *AIAA Paper* 83-0265, 1983.

[6] Baldwin, B. S., and Lomax, H., "Thin Layer Approximation and Algebraic Model for Separated Flows," *AIAA Paper* 78-257, 1978.

[7] Slomski, J. F., Gorski, J. J, Miller, R. W., Marino, T. A., "Numerical Simulation of Circulation Control Airfoils as Affected by Turbulence Models," *AIAA Paper* 02-0851, 2002.

[8] Paterson, E. G, and Baker, W. J., "Simulation of Steady Circulation Control for Marine-Vehicle Control Surfaces," *AIAA Paper* 04-0748, 2004.

[9] Abramson, J., "Two-Dimensional Subsonic Wind Tunnel Evaluation of Two Related Cambered 15-Percent Circulation Control Airfoils," DTNSRDC ASED-373, 1977.

[10] Krist, S. L., Biedron R. T. and Rumsey, C. L., "CFL3D User's Manual," *NASA TM* 1998-208444, 1998.

[11] Spalart, P. R. and Allmaras, S. R., "A One-Equation Turbulence Model for Aerodynamic Flows," *La Recherche Aerospatiale*, vol. 1, pp. 5–21, 1994.

[12] Spalart, P. R. and Shur, M., "On the Sensitization of Turbulence Models to Rotation and Curvature," *Aerospace Sci. Technol.*, vol. 5, pp. 297–302, 1997.

[13] Rumsey, C. L., Gatski, T. B., Anderson, W. K. and Nielsen, E. J., "Isolating Curvature Effects in Computing Wall-Bounded Turbulent Flows," *Inter. J. of Heat and Fluid Flow*, vol. 22, pp. 573–582, 2001.

[14] Menter, F. R., "Improved Two-Equation $k-\omega$ Turbulence Model for Aerodynamic Flows," *NASA TM* 103975, 1992.

[15] Menter, F. R., "Zonal Two Equation $k-\omega$ Turbulence Model for Aerodynamic Flows," *AIAA Paper* 93-2906, 1993.

[16] Menter, F. R., "Two-Equation Eddy-Viscosity Turbulence Models for Engineering Applications," *AIAA J.* vol. 32, No. 8, pp. 1598–1605, 1994.

[17] Rumsey, C. L., Gatski, T. B. and Morrison, J. H., "Turbulence Model Predictions of Strongly Curved Flow in a U-Duct," *AIAA J.*, vol. 38, No. 8, pp. 1394–1402, 2000.

[18] Menter, F. R., Kuntz, M. and Langtry, R., "Ten Years of Industrial Experience with the SST Turbulence Model," *Turbulence, Heat and Mass Transfer 4*, K. Hanjalic, Y. Nagano, and M. Tummers (editiors), Begell House, Inc., pp. 625–632, 2003.

[19] Turkel, T., Vatsa, V. N. and Radespiel, R., "Preconditioning Methods for Low-Speed Flow," *AIAA* , 96-2460, 1996.

[20] Turkel, T., Radespiel, R. and Kroll, N., "Assessment of Two Preconditioning Methods for Aerodynamic Problems," *Computers and Fluids*, vol. 26, no. 6, pp. 613–634, 1997.

[21] Turkel, T., "Preconditioning Techniques in Computational Fluid Dynamics," *Annual Review of Fluid Mechanics*, vol. 31, pp. 385–416, 1999.

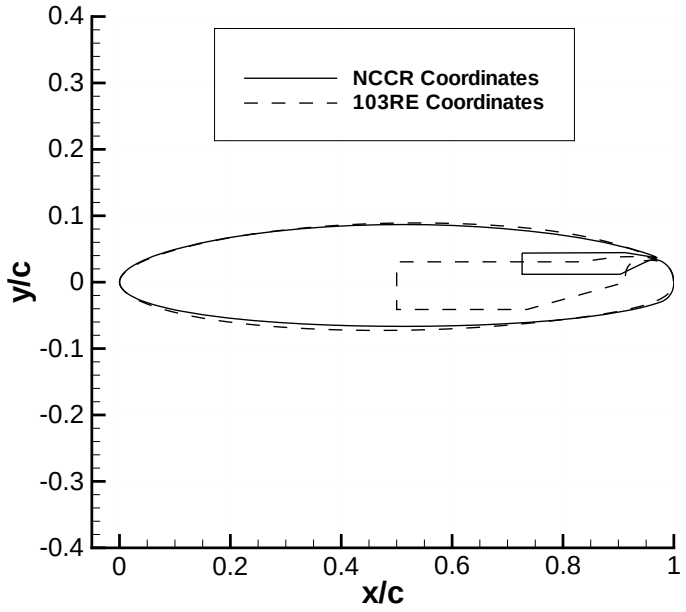

Figure 1: Geometry of airfoils.

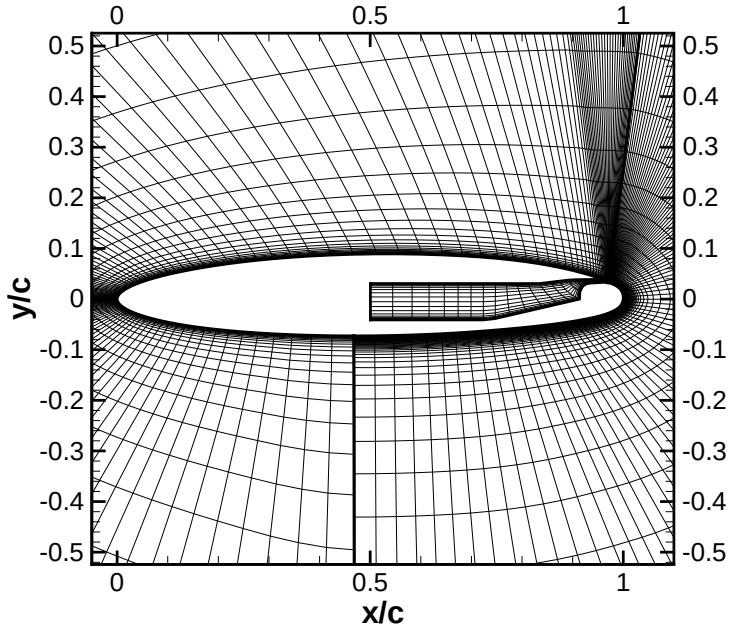

Figure 2: Near field of medium grid for circulation control airfoil.

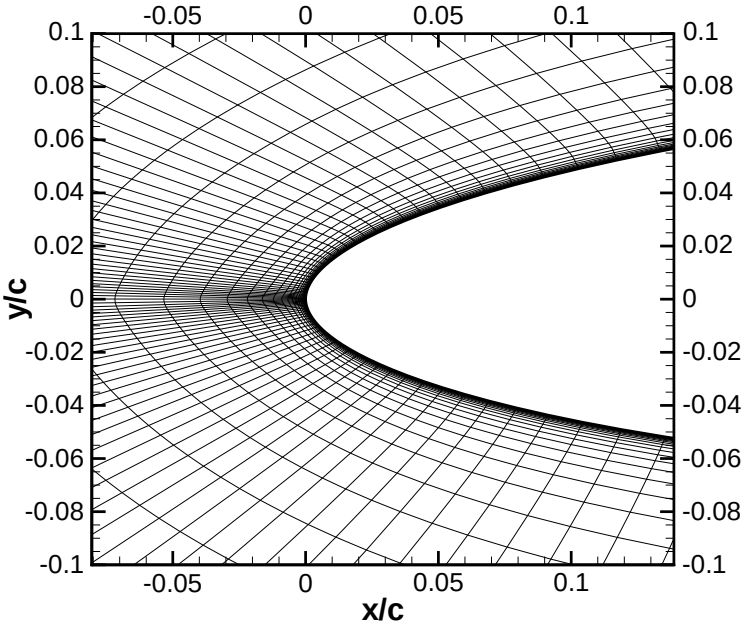

Figure 3: Leading edge region of medium grid for circulation control airfoil.

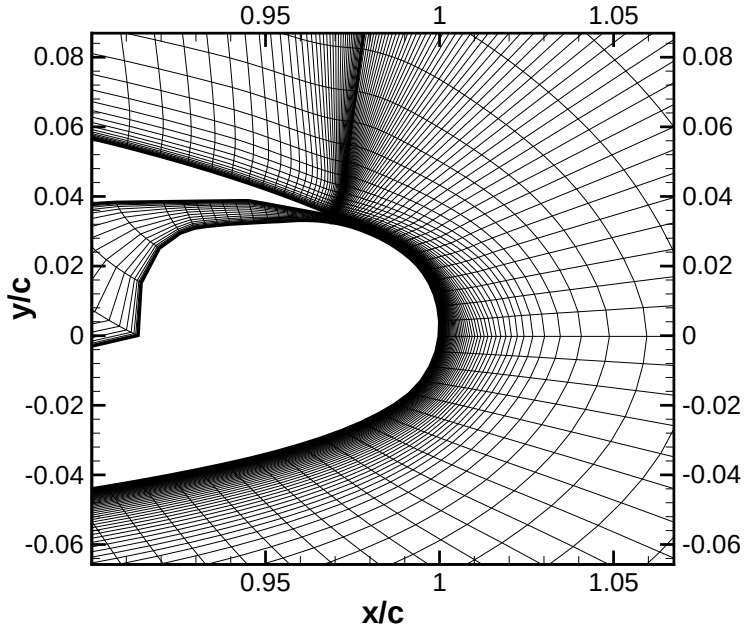

Figure 4: Trailing edge region of medium grid for circulation control airfoil.

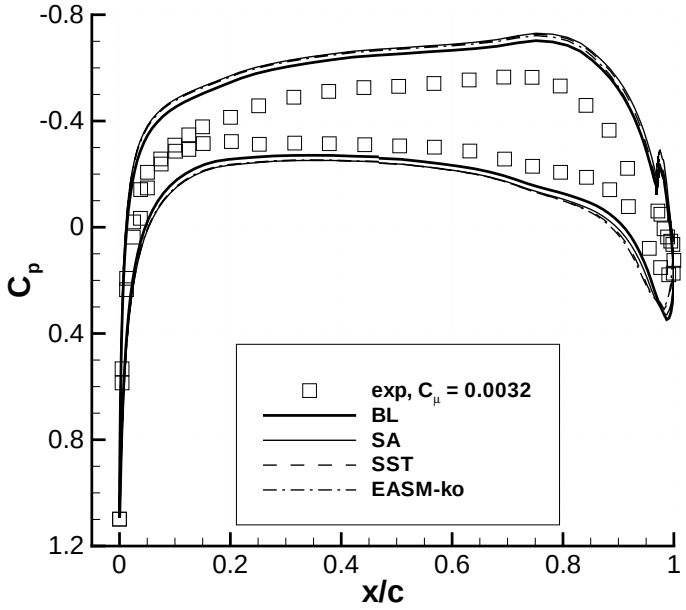

Figure 5: Comparison of surface pressures computed with several turbulence models ($M_\infty = 0.6$, $\alpha = 0°$, $Re_c = 5.2 \times 10^6$, $C_\mu = 0.0032$, medium grid).

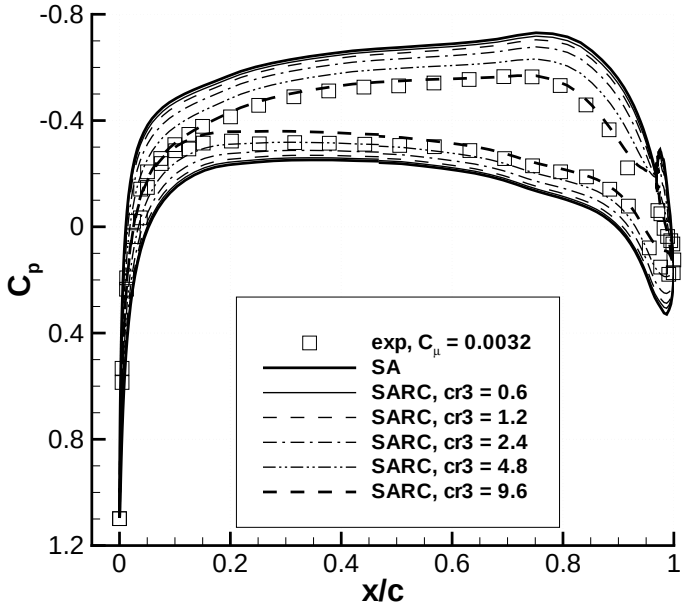

Figure 6: Effect of turbulence production parameter c_{r3} of SARC model on surface pressures ($M_\infty = 0.6$, $\alpha = 0°$, $Re_c = 5.2 \times 10^6$, $C_\mu = 0.0032$, medium grid).

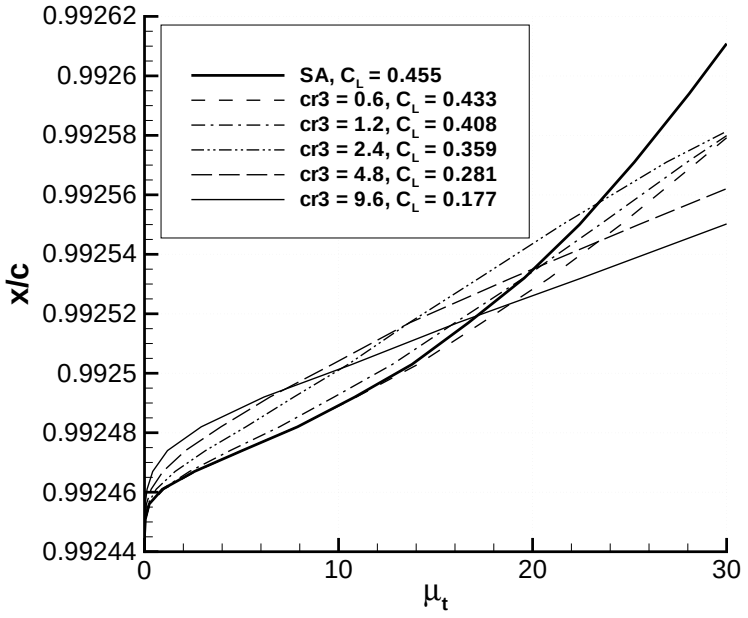

Figure 7: Effect of turbulence production parameter c_{r3} of SARC model on turbulent viscosity ($M_\infty = 0.6$, $\alpha = 0°$, $Re_c = 5.2 \times 10^6$, $C_\mu = 0.0032$, medium grid).

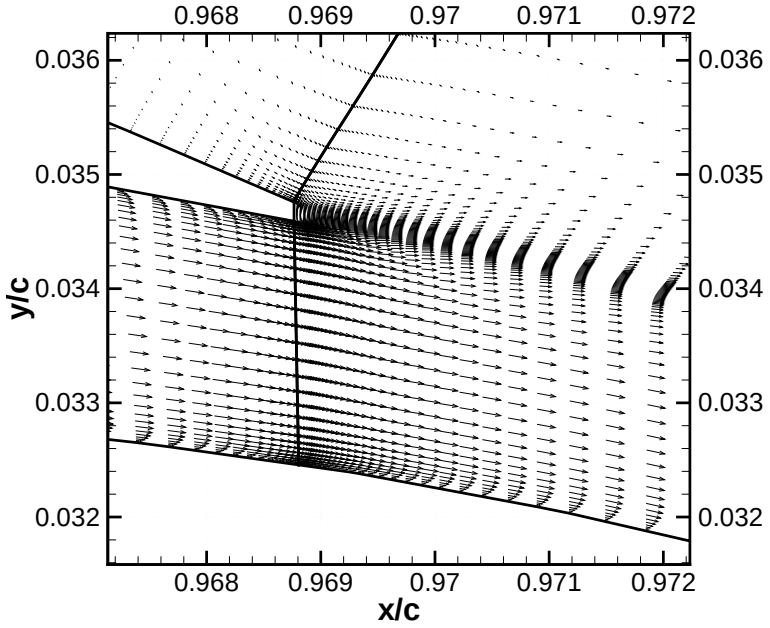

Figure 8: Velocity vectors near jet exit computed with SARC model and $c_{r3} = 9.6$ ($M_\infty = 0.6$, $\alpha = 0°$, $Re_c = 5.2 \times 10^6$, $C_\mu = 0.0032$, medium grid).

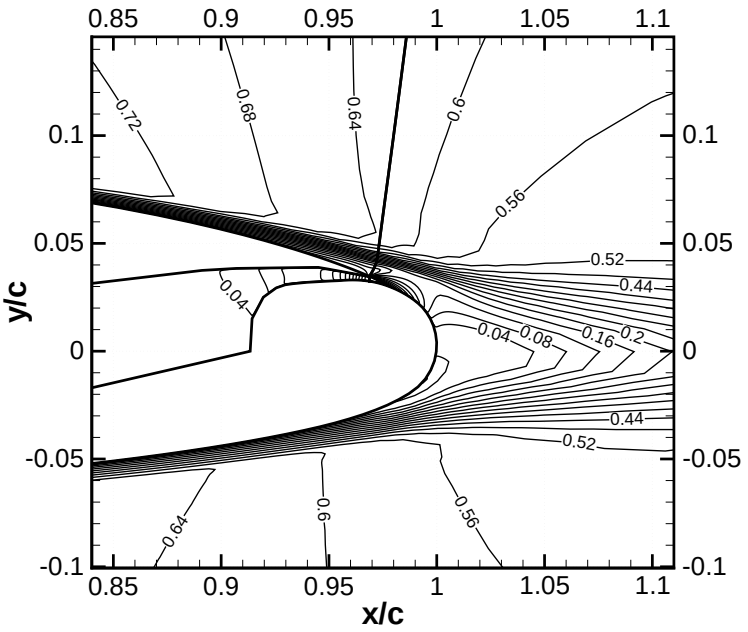

Figure 9: Mach contours at trailing edge computed with SARC model and $c_{r3} = 9.6$ ($M_\infty = 0.6$, $\alpha = 0°$, $Re_c = 5.2 \times 10^6$, $C_\mu = 0.0032$, medium grid).

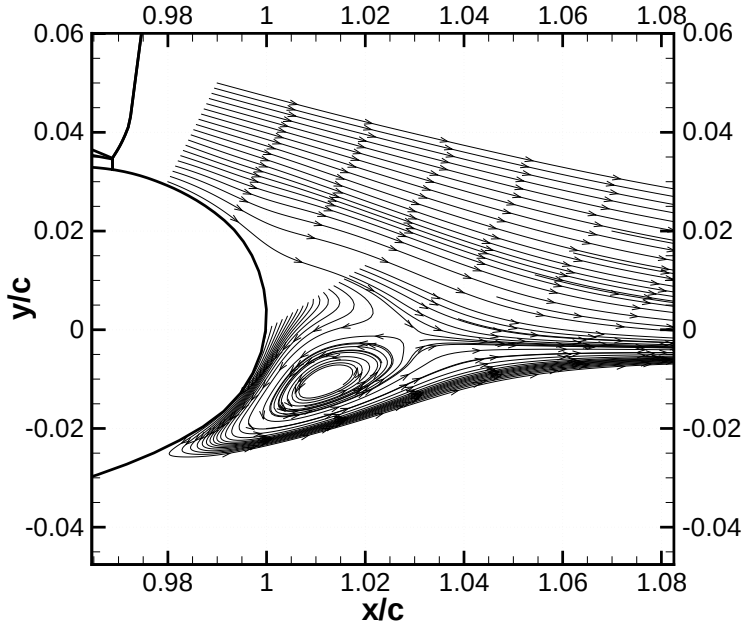

Figure 10: Streamline pattern at trailing edge computed with SARC model and $cr3 = 9.6$ ($M_\infty = 0.6$, $\alpha = 0°$, $Re_c = 5.2 \times 10^6$, $C_\mu = 0.0032$, medium grid).

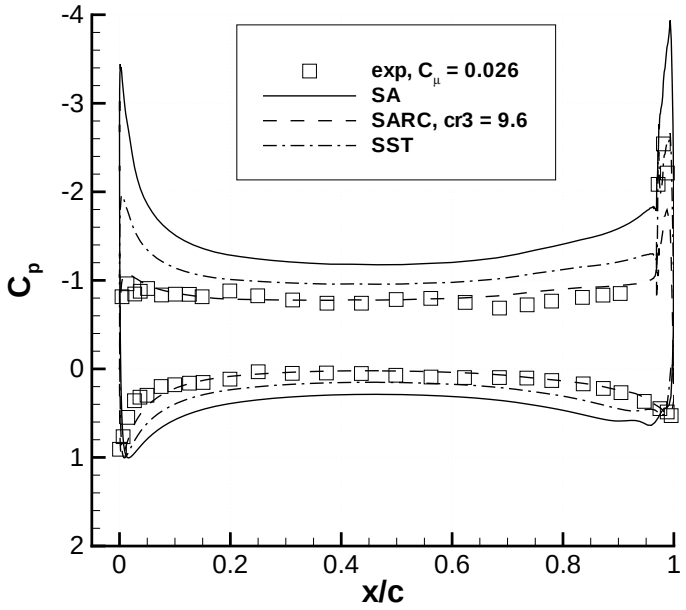

Figure 11: Surface pressures computed with SA, SARC($c_{r3} = 9.6$), and SST turbulence models ($M_\infty = 0.12$, $\alpha = 0°$, $Re_c = 5.45 \times 10^5$, $C_\mu = 0.026$, medium grid).

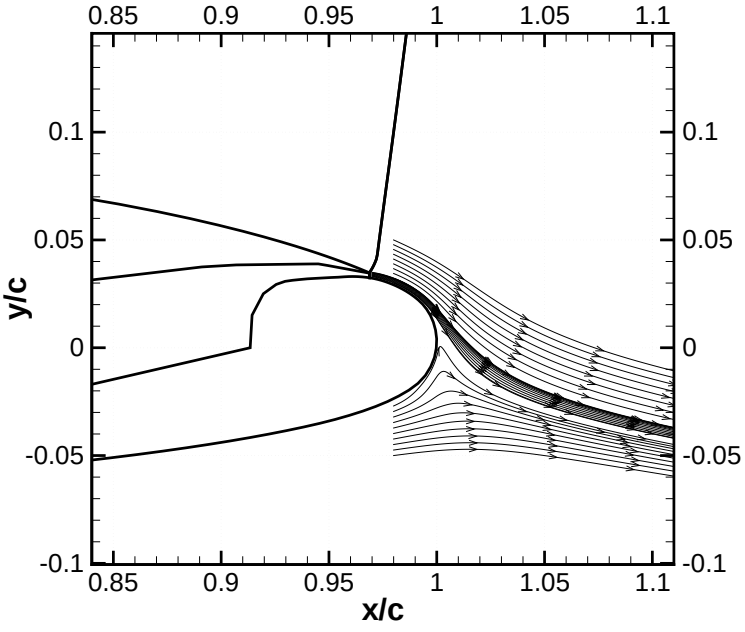

Figure 12: Jet streamlines computed with SARC($c_{r3} = 9.6$) turbulence model ($M_\infty = 0.12$, $\alpha = 0°$, $Re_c = 5.45 \times 10^5$, $C_\mu = 0.026$, medium grid).

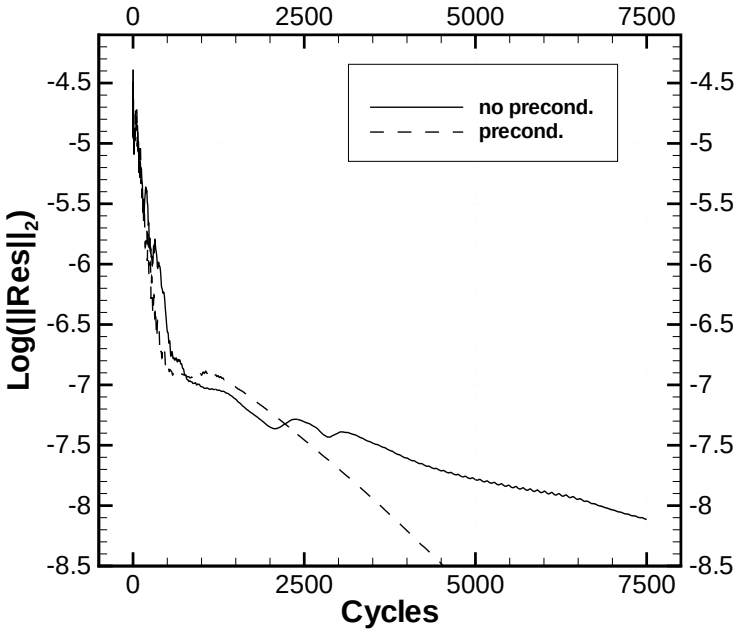

Figure 13: Residual histories with SA turbulence model, without and with preconditioning ($M_\infty = 0.12$, $\alpha = 0°$, $Re_c = 5.45 \times 10^5$, $C_\mu = 0.026$, medium grid).

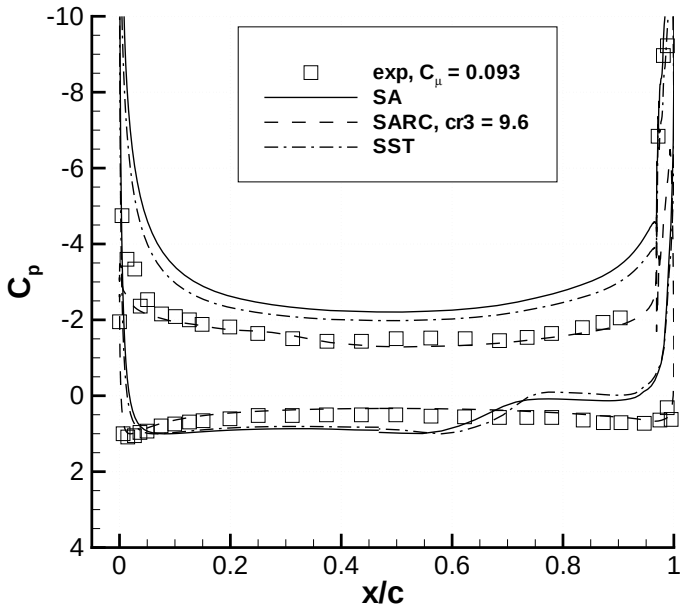

Figure 14: Surface pressures computed with SA, SARC($c_{r3} = 9.6$), and SST turbulence models ($M_\infty = 0.12$, $\alpha = 0°$, $Re_c = 5.45 \times 10^5$, $C_\mu = 0.093$, medium grid).

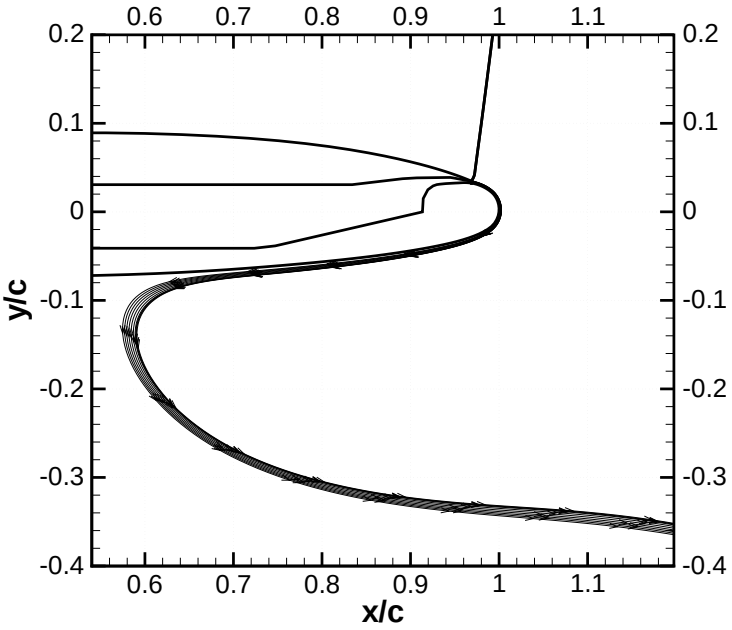

Figure 15: Jet streamlines computed with SA turbulence model ($M_\infty = 0.12$, $\alpha = 0°$, $Re_c = 5.45 \times 10^5$, $C_\mu = 0.093$, medium grid).

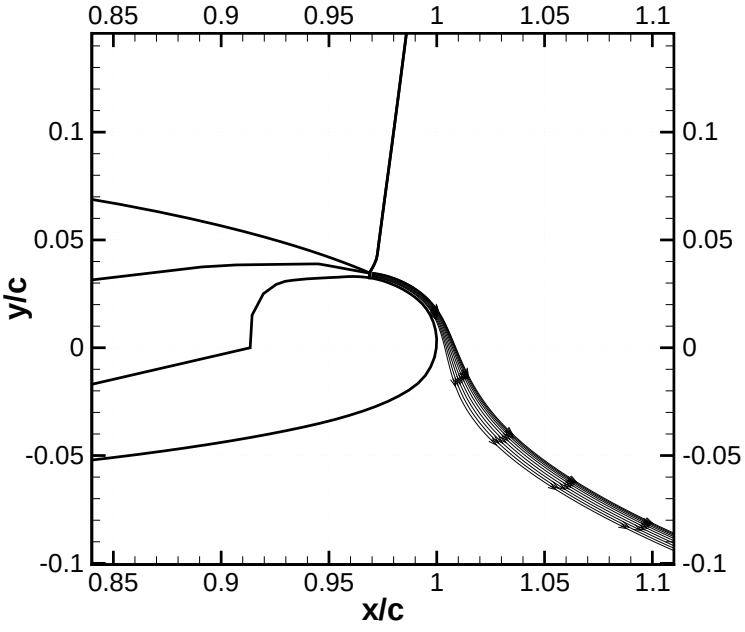

Figure 16: Jet streamlines computed with SARC($c_{r3} = 9.6$) turbulence model ($M_\infty = 0.12$, $\alpha = 0°$, $Re_c = 5.45 \times 10^5$, $C_\mu = 0.093$, medium grid).

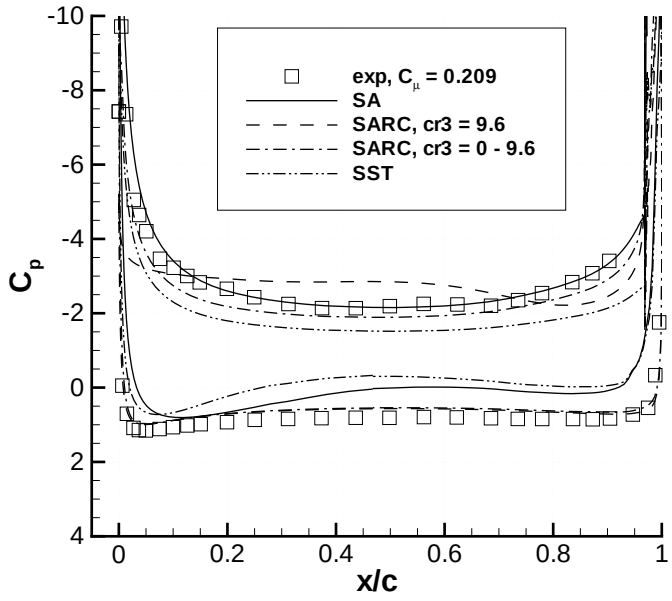

Figure 17: Surface pressures computed with SA, SARC($c_{r3} = 9.6$), SARC($c_{r3} = 0 - 9.6$), and SST turbulence models ($M_\infty = 0.12$, $\alpha = 0°$, $Re_c = 5.45 \times 10^5$, $C_\mu = 0.209$, medium grid).

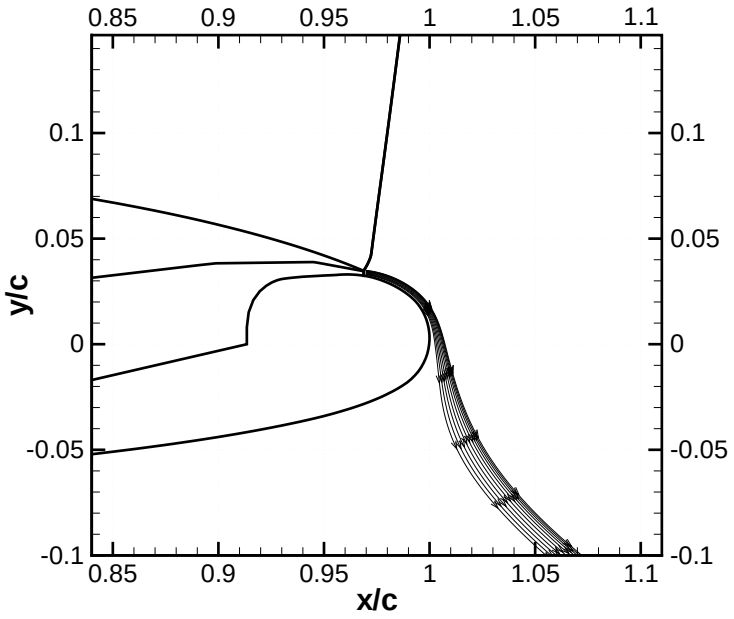

Figure 18: Jet streamlines computed with SARC($c_{r3} = 0 - 9.6$) turbulence model ($M_\infty = 0.12$, $\alpha = 0°$, $Re_c = 5.45 \times 10^5$, $C_\mu = 0.209$, fine grid).

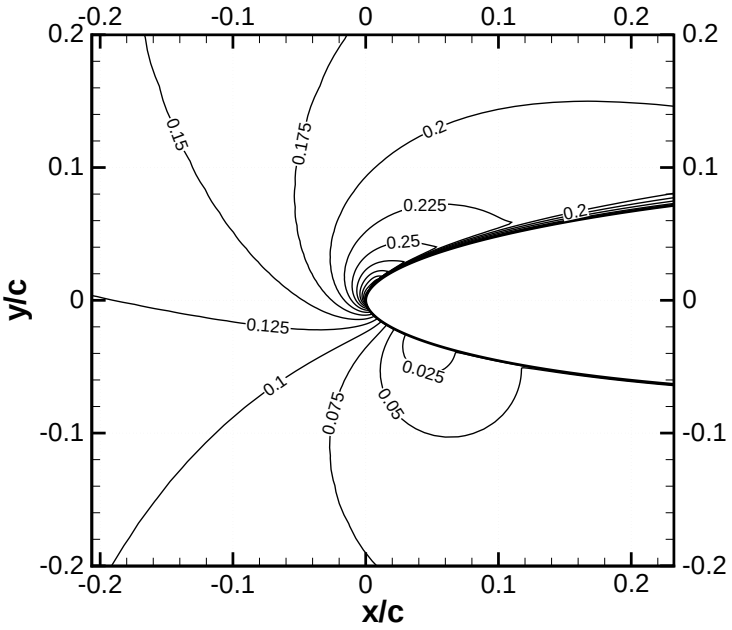

Figure 19: Mach contours computed at leading edge with SARC($c_{r3} = 0 - 9.6$) turbulence model ($M_\infty = 0.12$, $\alpha = 0^\circ$, $Re_c = 5.45 \times 10^5$, $C_\mu = 0.209$, fine grid).

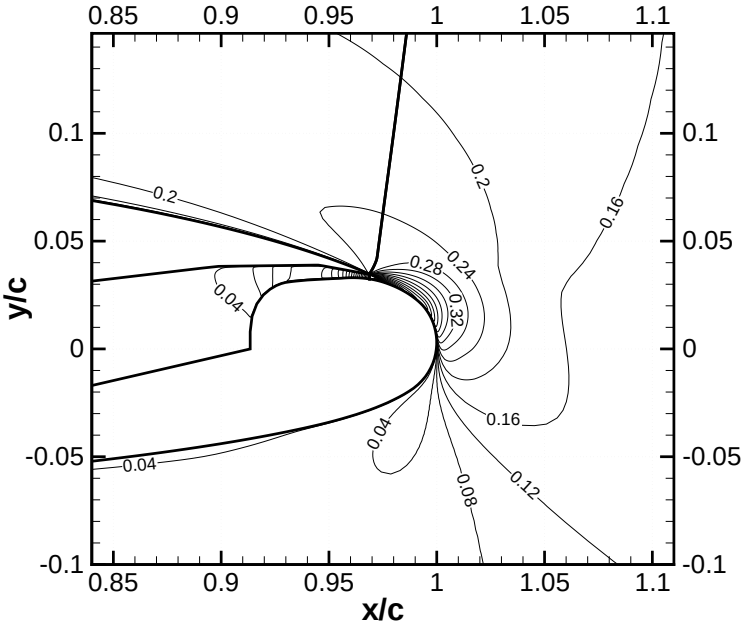

Figure 20: Mach contours computed at trailing edge with SARC($c_{r3} = 0 - 9.6$) turbulence model ($M_\infty = 0.12$, $\alpha = 0^\circ$, $Re_c = 5.45 \times 10^5$, $C_\mu = 0.209$, fine grid).

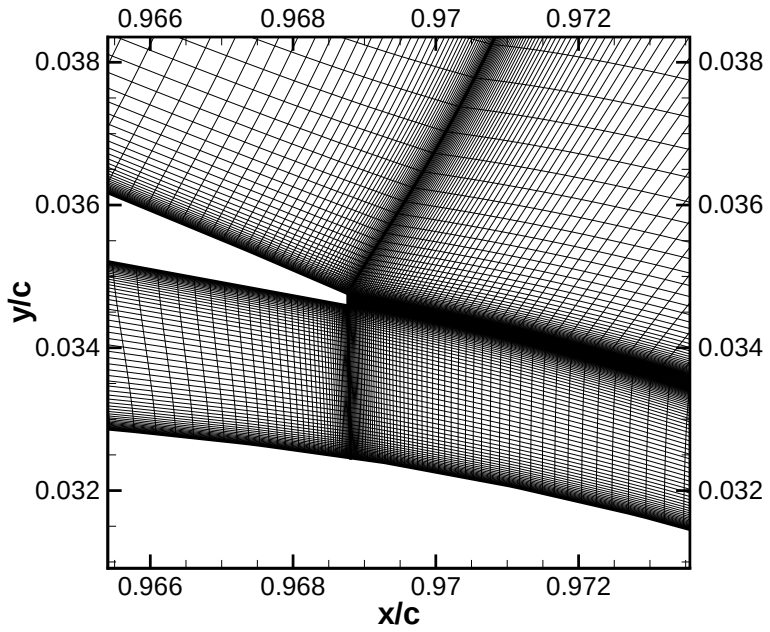

Figure 21: Fine grid in jet exit region.

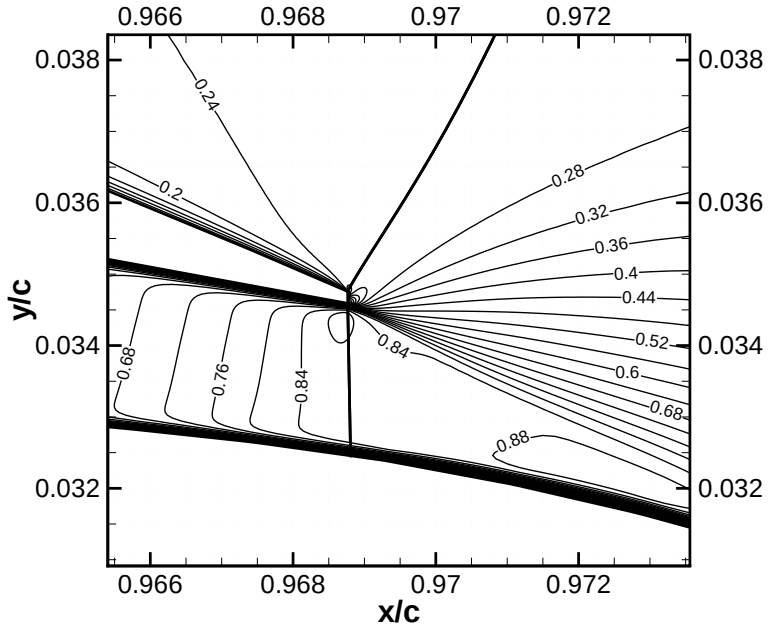

Figure 22: Mach contours in the vicinity of jet exit computed with SARC($c_{r3} = 0 - 9.6$) turbulence model ($M_\infty = 0.12$, $\alpha = 0°$, $Re_c = 5.45 \times 10^5$, $C_\mu = 0.209$, fine grid).

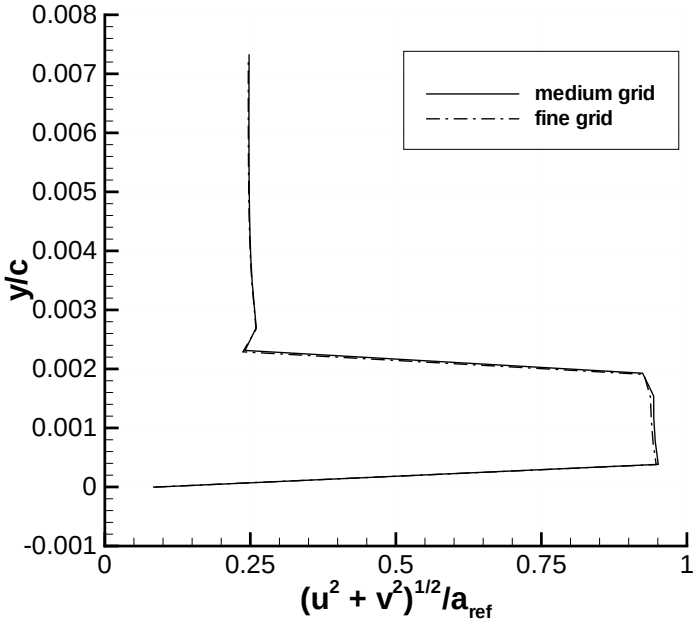

Figure 23: Effect of mesh density on velocity profiles computed at jet exit with SARC($c_{r3} = 0 - 9.6$) turbulence model ($M_\infty = 0.12$, $\alpha = 0°$, $Re_c = 5.45 \times 10^5$, $C_\mu = 0.209$).

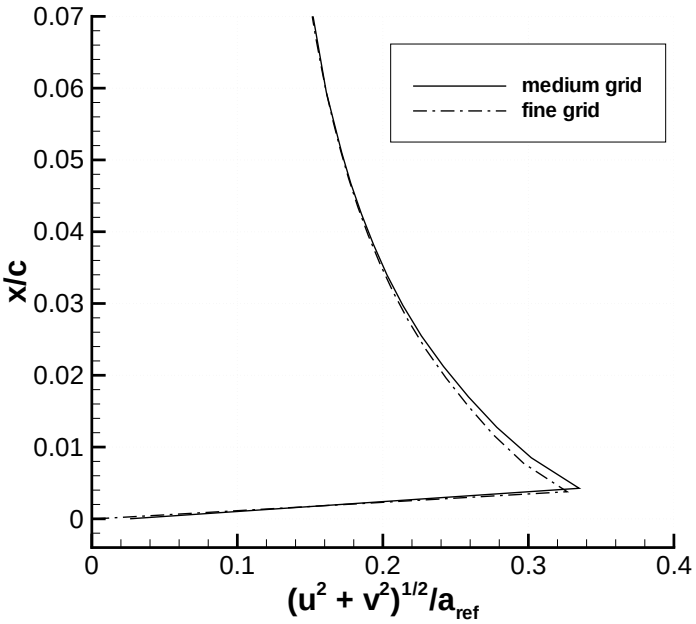

Figure 24: Effect of mesh density on velocity profiles computed at trailing edge with SARC($c_{r3} = 0 - 9.6$) turbulence model ($M_\infty = 0.12$, $\alpha = 0°$, $Re_c = 5.45 \times 10^5$, $C_\mu = 0.209$).

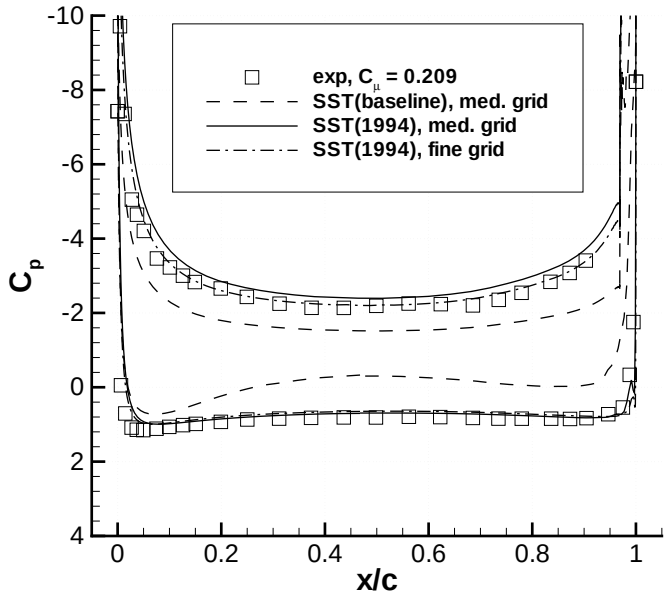

Figure 25: Surface pressures computed with SST(1994) turbulence model ($M_\infty = 0.12$, $\alpha = 0°$, $Re_c = 5.45 \times 10^5$, $C_\mu = 0.209$).

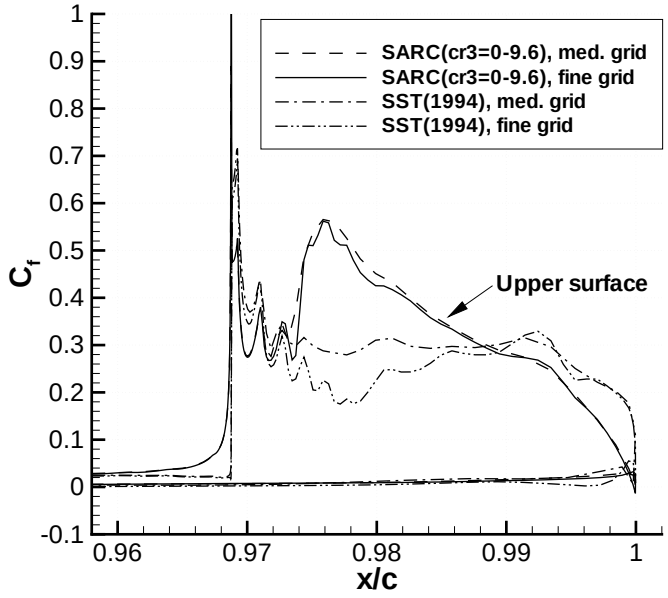

Figure 26: Comparison of surface skin-friction distributions at the trailing edge computed with SARC($c_{r3} = 0 - 9.6$) and SST(1994) turbulence models ($M_\infty = 0.12$, $\alpha = 0°$, $Re_c = 5.45 \times 10^5$, $C_\mu = 0.209$).

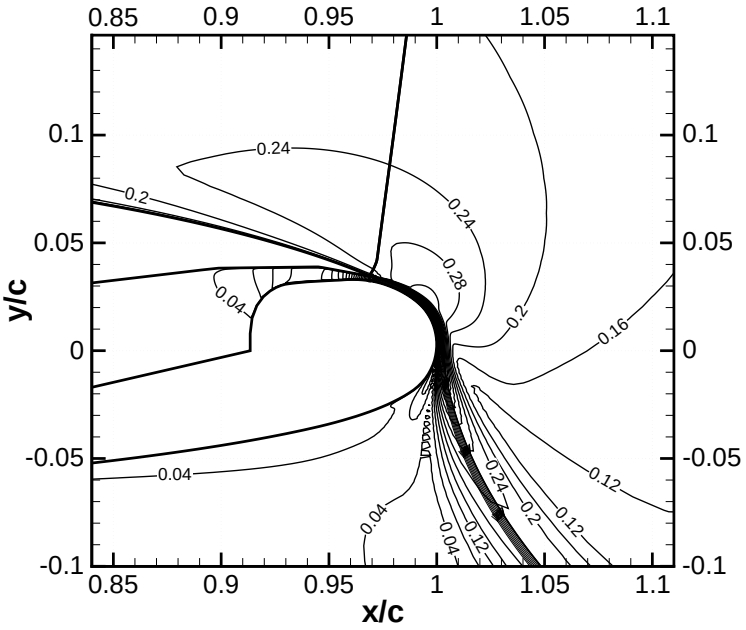

Figure 27: Jet streamlines and Mach contours computed with SST(1994) turbulence model ($M_\infty = 0.12$, $\alpha = 0°$, $Re_c = 5.45 \times 10^5$, $C_\mu = 0.209$, fine grid).

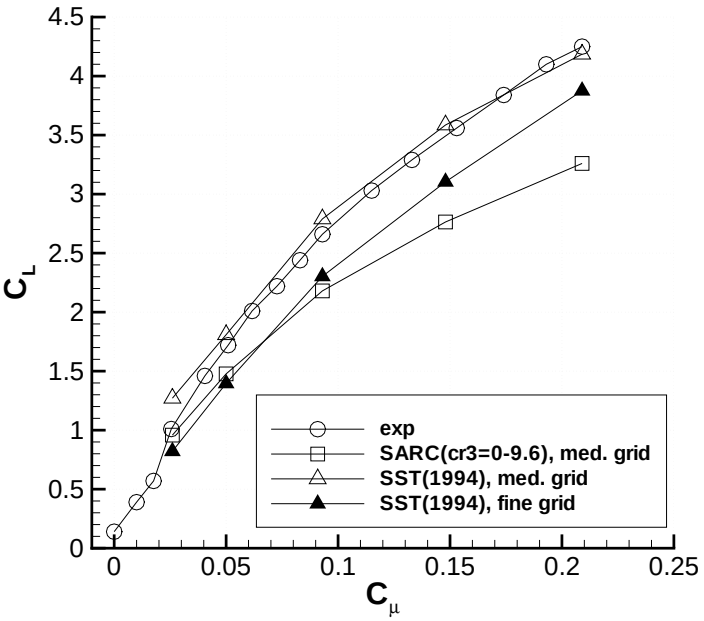

Figure 28: Variation of lift coefficient with jet momentum coefficient using SARC($c_{r3} = 0 - 9.6$) and SST(1994) turbulence models ($M_\infty = 0.12$, $\alpha = 0°$, $Re_c = 5.45 \times 10^5$).

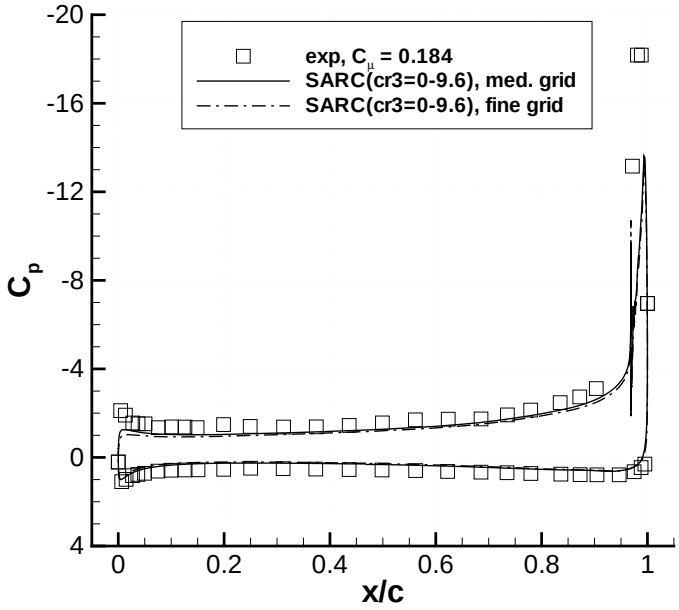

Figure 29: Surface pressures computed with SARC($c_{r3} = 0 - 9.6$) turbulence model ($M_\infty = 0.12$, $\alpha = -8°$, $Re_c = 5.45 \times 10^5$, $C_\mu = 0.184$).

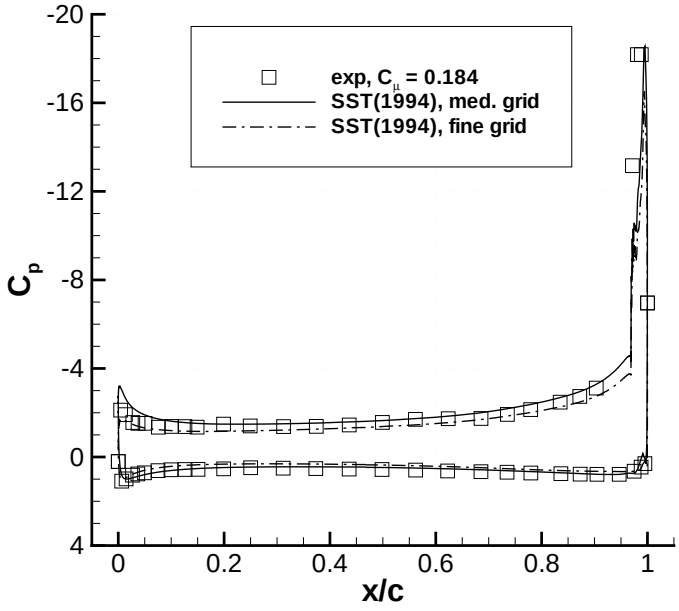

Figure 30: Surface pressures computed with SST(1994) turbulence model ($M_\infty = 0.12$, $\alpha = -8°$, $Re_c = 5.45 \times 10^5$, $C_\mu = 0.184$).

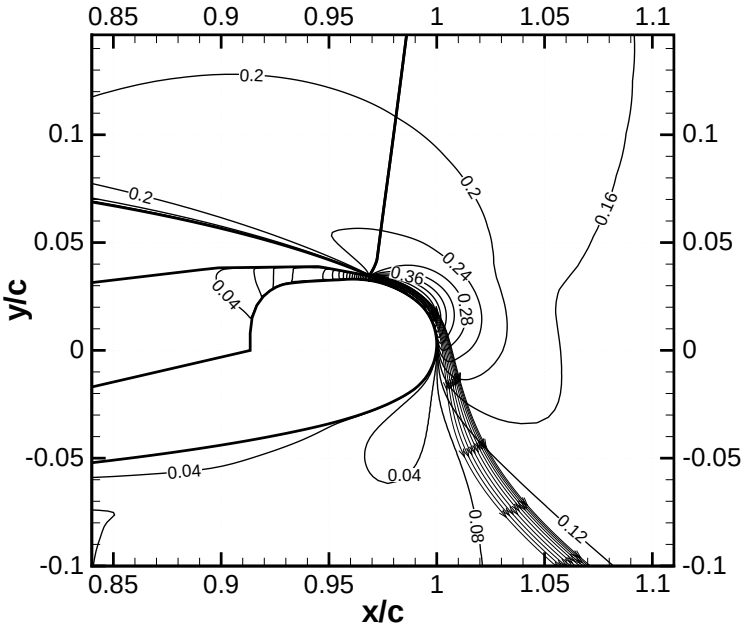

Figure 31: Jet streamlines and Mach contours computed at trailing edge with SARC($c_{r3} = 0 - 9.6$) turbulence model ($M_\infty = 0.12$, $\alpha = -8°$, $Re_c = 5.45 \times 10^5$, $C_\mu = 0.184$), fine grid).

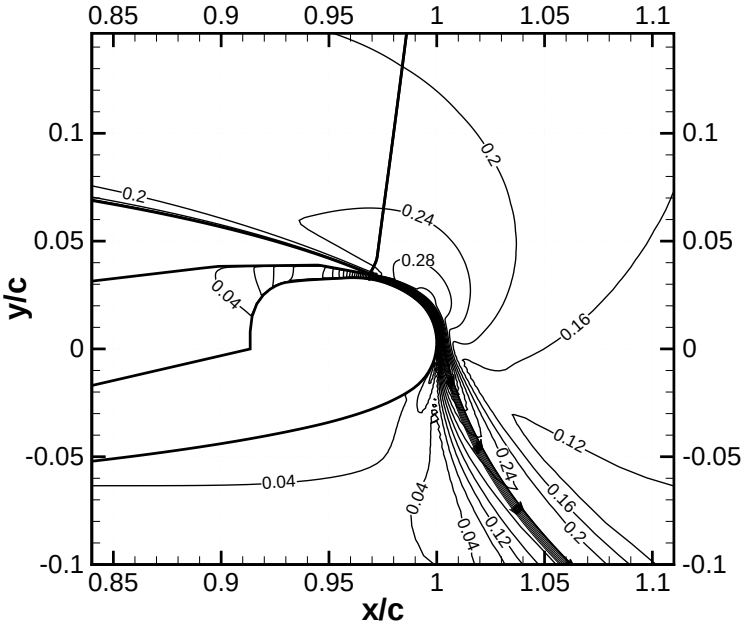

Figure 32: Jet streamlines and Mach contours computed at trailing edge with SST(1994) turbulence model ($M_\infty = 0.12$, $\alpha = -8°$, $Re_c = 5.45 \times 10^5$, $C_\mu = 0.184$, fine grid).

Aspects of Numerical Simulation of Circulation Control Airfoils

R. C. Swanson, C. L. Rumsey, S. G. Anders
NASA Langley Research Center

2004 Circulation Control Workshop (March 16 - 17)

Outline

- Introduction
  - Motivation and objectives
  - Definition of jet momentum coefficient
- Computational Method
- Turbulence Modeling
- Geometry, flow conditions, grid
- Computational Results
  - Initial effort ($M_\infty = 0.6$, $Re_c = 5.2 \times 10^6$)
  - Workshop cases ($M_\infty = 0.12$, $Re_c = 5.45 \times 10^5$)
- Conclusions

Introduction

- Some possible benefits of circulation control airfoils (e.g., for general aviation)
  - Reduced weight and complexity (maintenance) relative to conventional high lift systems
  - Slower takeoff and landing speeds
  - Increased maneuverability
- There is a need to develop reliable flow prediction capability.
- Key issue for computing circulation control airfoil flows is turbulence modeling.

Introduction (Cont.)

- Previous work (on the workshop cases), indicates uncertainty in required turbulence model complexity.
  - Full Reynolds stress model (Slomski et al., 2002)
  - Two transport equations (Paterson and Baker, 2004)
- Computational efficiency and reliability is another important issue for computing circulation control airfoil flows.
  - Convergence acceleration (steady flows)
  - Improved efficiency of time integration scheme (unsteady flows)
  - Numerical compatibility of turbulence model

Introduction (Cont.)

- Capability of flow prediction tool must include:
  - Accurate prediction of details of flow (i.e., velocity profiles, Reynolds stresses, TKE, jet characteristics)
  - Pulsating jets, multiple jets
  - Amenable to broad range of flow conditons (i.e., M_∞, Re_∞, α)
  - 3-D effects
- In current effort various aspects of computing circulation control airfoils are considered.
  - Turbulence modeling
  - Flow conditions
  - Grid density
  - Variation of lift with jet momentum coefficient (C_μ)
  - Convergence behavior

Jet Momentum Coefficient

- Definition

$$C_\mu = \frac{\dot{m}_j V_j}{\frac{1}{2}\rho_\infty {V_\infty}^2 S} = \frac{\rho_j {V_j}^2 hb}{\frac{1}{2}\rho_\infty {V_\infty}^2 cb}$$

- $C_\mu \sim {M_\infty}^{-2}$
- Assume the same jet conditions. Then (roughly) for $M_\infty = 0.12$ and $M_\infty = 0.6$

$$(C_\mu)_{M=0.6} \approx \frac{(C_\mu)_{M=0.12}}{25}$$

- One must keep this in mind when interpreting C_μ as M_∞ increases.

Computational Method

- Computer Code: CFL3D (developed at NASA Langley)
- Solves mass-averaged Navier-Stokes equations
- Allows multi-zone domain
- Grids: one-to-one, patched, or overset
- Finite-volume discretization method
  - Flux difference splitting scheme of Roe
  - 3rd-order upwind biased differencing, convective terms
  - central differencing, pressure and viscous terms
- Time advancement: implicit AF scheme

Computational Method (cont)

- Solves steady and unsteady flows
  - Steady flows: Convergence acceleration with multigrid (FMG)
  - Unsteady flows: dual time stepping with subiterations and multigrid

Turbulence Modeling

- Baldwin-Lomax (BL): Zero equation (algebraic eddy viscosity model)
- Spalart-Allmaras (SA)
  - One equation model (1994)
  - Transport equation for eddy viscosity
- Spalart-Allmaras with curvature effects (SARC)
- Shear stress transport (SST)
  - Two equation model (1992, Menter)
  - Transport of TKE and ω ($\sim$ dissipation rate)
- Explicit algebraic stress (EASM-ko)
  - Two equation model + algebraic eqns. (1993, Gatski and Speziale)

SARC Turbulence Model

- The SA model can be written in general form as

$$\frac{D\tilde{\nu}}{Dt} = \mathcal{P} + \mathcal{D}_{diff} + \mathcal{D}_{diss} \tag{1}$$

  where $\mathcal{P} = c_{b1}[1 - f_{t2}]W\tilde{\nu}$ and $\tilde{\nu} \sim \nu_t$.

- In the SARC model $\mathcal{P}$ is replaced by

$$\mathcal{P}' = c_{b1}[f_{r1} - f_{t2}]W\tilde{\nu} \tag{2}$$

$$f_{r1} = (1 + c_{r1})\frac{2r^*}{(1 + r^*)}\left[1 - c_{r3}\tan^{-1}(c_{r2}\tilde{r})\right] - c_{r1}, \tag{3}$$

Airfoil Geometry

- Workshop geometry: Elliptical airfoil (designated NCCR 1510-7067N),
  - Chord of 8 inches
  - 15% thickness ratio, 1% camber ratio
  - Slot height-to-chord ratio: $h/c = 0.0030$ ($h = 0.024$ inches)
- Geometry: Elliptical airfoil (designated 103RE or 103XW)
  - Chord of 18 inches
  - 16% thickness ratio, 1% camber ratio
  - Slot height-to-chord ratio: $h/c = 0.0021$ ($h = 0.0378$ inches)

Geometry of Elliptical Airfoils

Circulation Control Airfoils

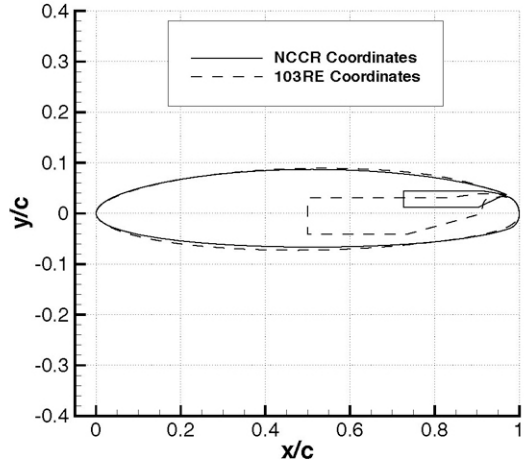

Flow Conditions

- High free-stream Mach number
  - $M_\infty = 0.6$, $Re_c = 5.2 \times 10^6$, $\alpha = 0°$
  - Case 302: $M_{\text{jet}} = 0.519$, $C_\mu = 0.0032$
- Low free-stream Mach number
  - $M_\infty = 0.12$, $Re_c = 5.45 \times 10^5$, $\alpha = 0°$
  - Case 283: $C_\mu = 0.209$
  - $M_\infty = 0.12$, $Re_c = 5.45 \times 10^5$, $\alpha = -8°$
  - Case 321: $C_\mu = 0.184$

Computational Grid

- Medium grid
  - Multiblock domain with 3 blocks
  - 235 grid points around the airfoil
  - 49 points in the normal direction over forward part of the airfoil
  - 101 points in the normal direction over aft part of the airfoil (includes points in nozzle)
- Fine grid: number of grid cells doubled in each coordinate direction (70,563 points)

Computational Grid

Circulation Control Airfoil

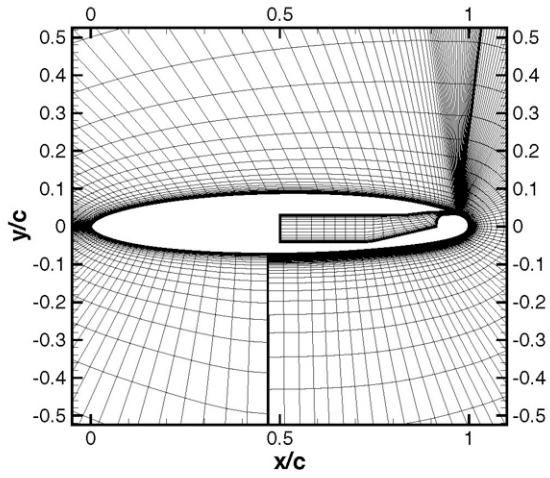

Computational Grid

Medium Grid, Leading and Trailing Edges

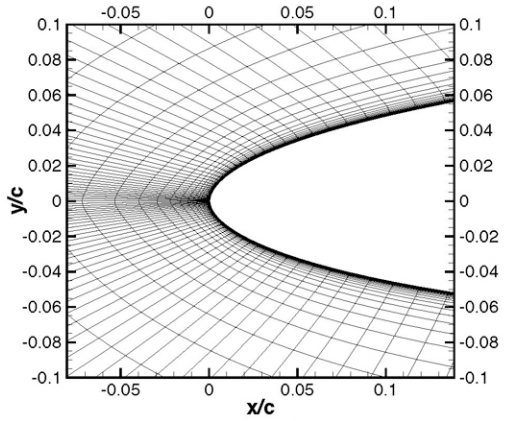

(a) Leading edge

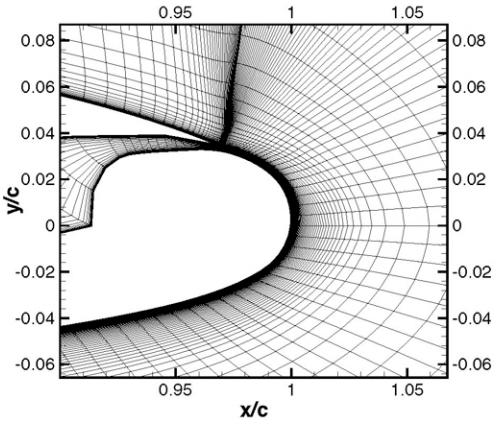

(b) Trailing edge

Surface Pressures (Case 302)

$M_\infty = 0.6,\ \alpha = 0^\circ,\ Re_c = 5.2 \times 10^6,\ C_\mu = 0.0032,\ C_L = 0.191$

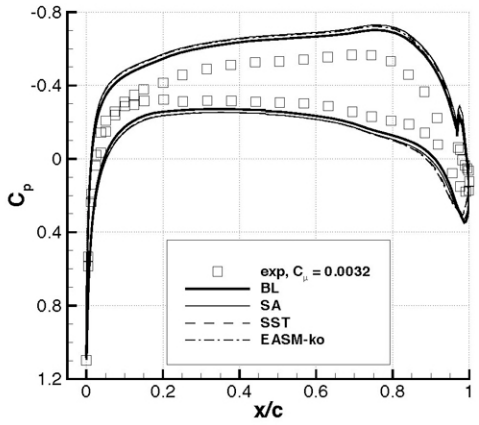

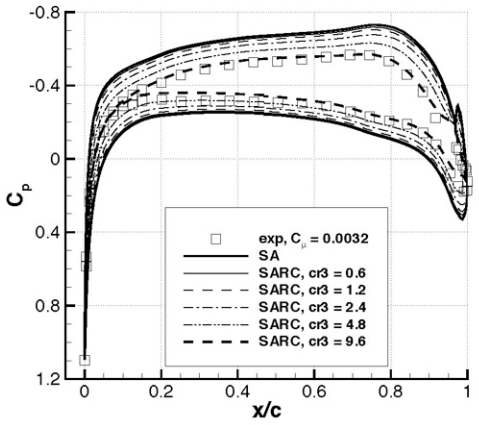

Streamline Pattern at Trailing Edge

$M_\infty = 0.6,\ \alpha = 0^\circ,\ Re_c = 5.2 \times 10^6,\ C_\mu = 0.0032$

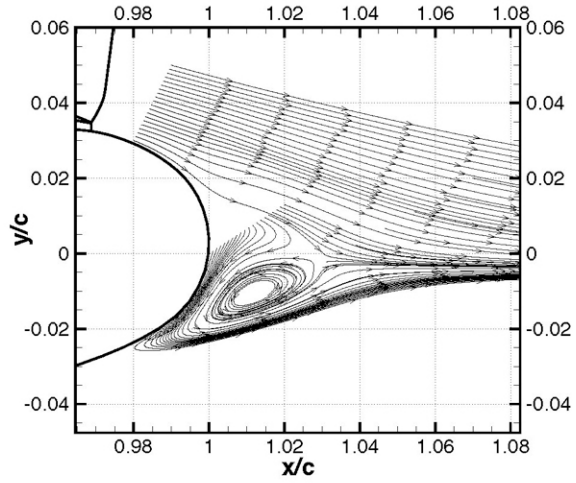

Effect of Model Constant on Turbulent Viscosity

$M_\infty = 0.6,\ \alpha = 0°,\ Re_c = 5.2 \times 10^6,\ C_\mu = 0.0032$

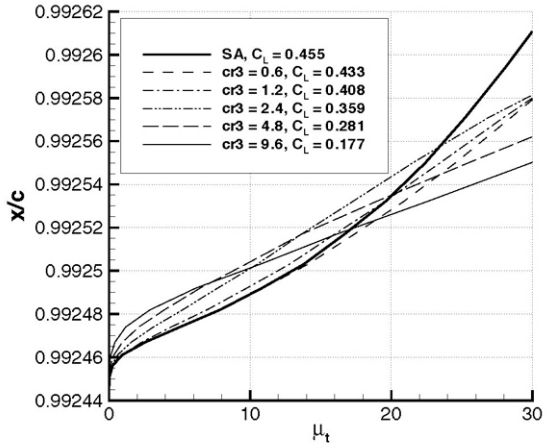

Influence of Turbulence Model on Separation

$M_\infty = 0.6,\ \alpha = 0°,\ Re_c = 5.2 \times 10^6$

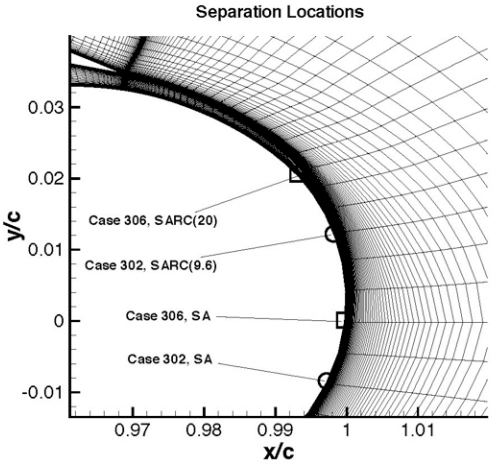

Surface Pressures and Jet Streamlines

$M_\infty = 0.12,\ \alpha = 0^\circ,\ Re_c = 5.45 \times 10^5,\ C_\mu = 0.026$

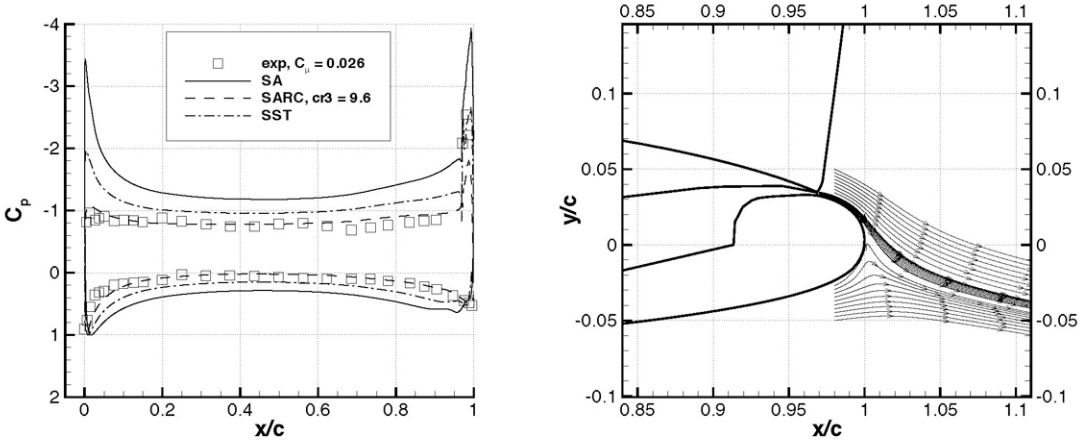

Convergence Behavior with SA Model

$M_\infty = 0.12,\ \alpha = 0^\circ,\ Re_c = 5.45 \times 10^5,\ C_\mu = 0.026$

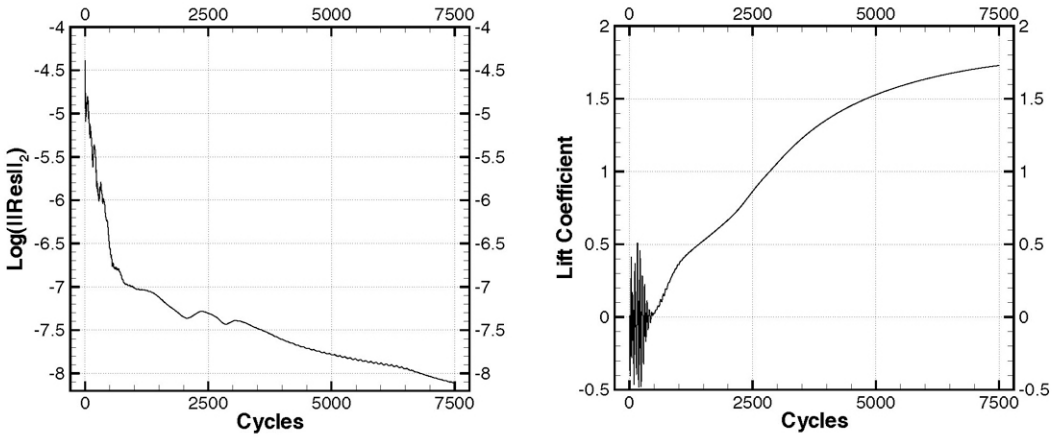

Surface Pressures

$M_\infty = 0.12,\ \alpha = 0°,\ Re_c = 5.45 \times 10^5,\ C_\mu = 0.093$

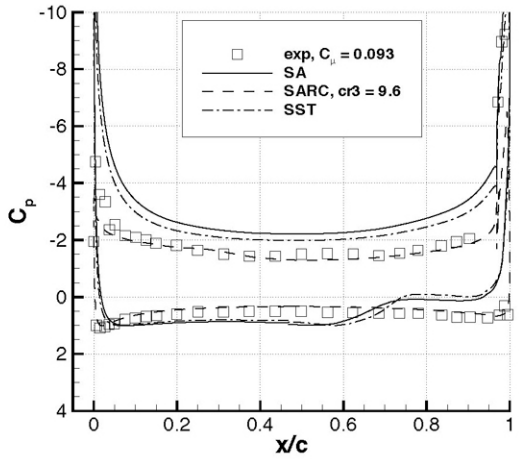

Jet Streamlines - SA and SARC Models

$M_\infty = 0.12,\ \alpha = 0°,\ Re_c = 5.45 \times 10^5,\ C_\mu = 0.093$

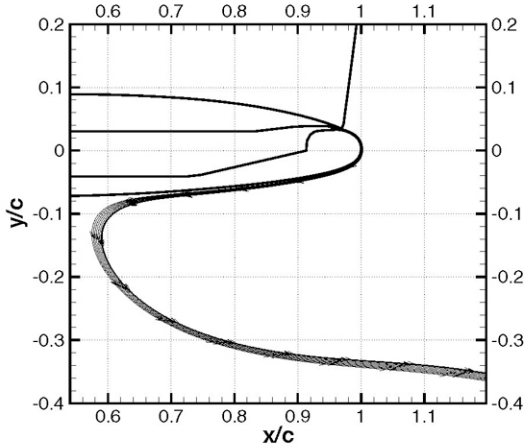

(a) SA

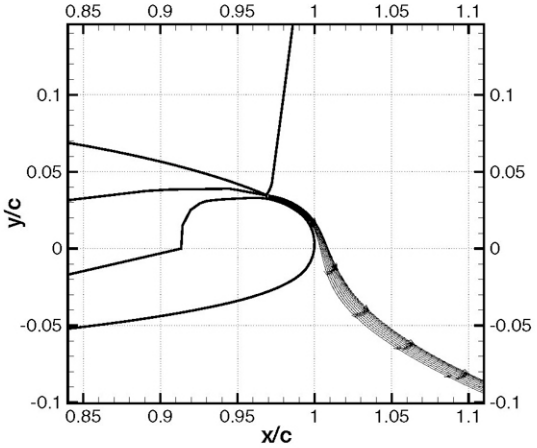

(b) SARC($cr3 = 9.6$)

Surface Pressures and Jet Streamlines (Case 283)

$M_\infty = 0.12,\ \alpha = 0^\circ,\ Re_c = 5.45 \times 10^5,\ C_\mu = 0.209$

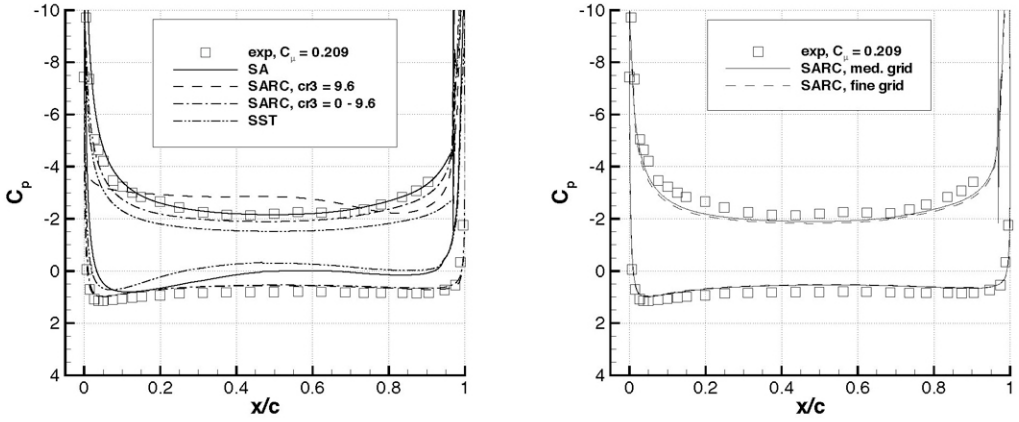

Jet Streamlines (Case 283)

$M_\infty = 0.12,\ \alpha = 0^\circ,\ Re_c = 5.45 \times 10^5,\ C_\mu = 0.209$

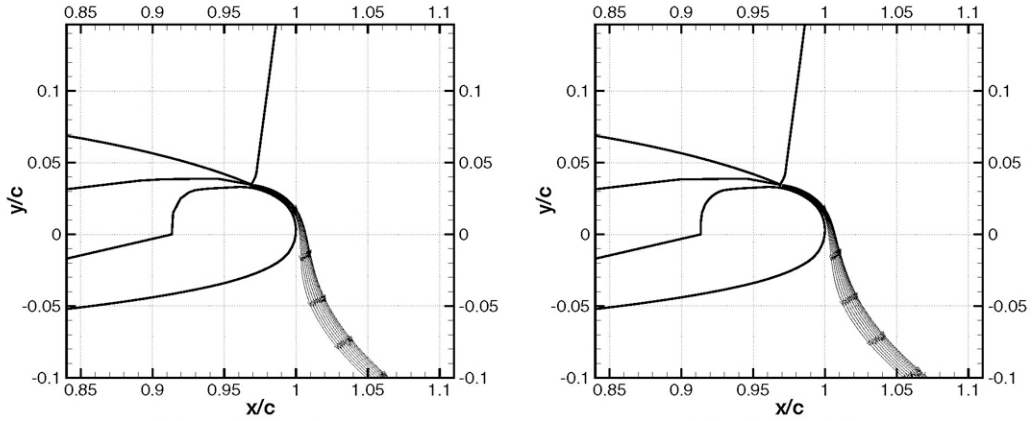

(a) Medium grid (b) Fine grid

Streamline Pattern at Trailing Edge

$M_\infty = 0.12,\ \alpha = 0^\circ,\ Re_c = 5.45 \times 10^5,\ C_\mu = 0.209$

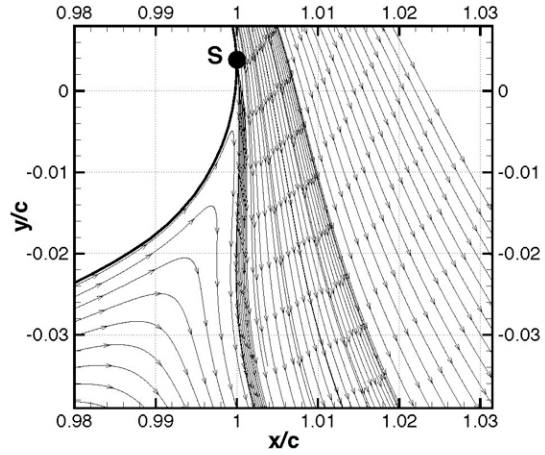

Effect of Mesh Density on Velocity Profiles

$M_\infty = 0.12,\ \alpha = 0^\circ,\ Re_c = 5.45 \times 10^5,\ C_\mu = 0.209$

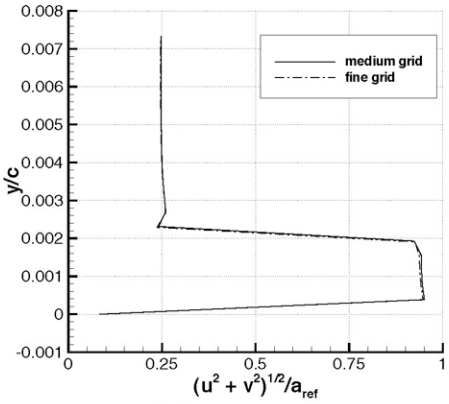

(a) Jet exit

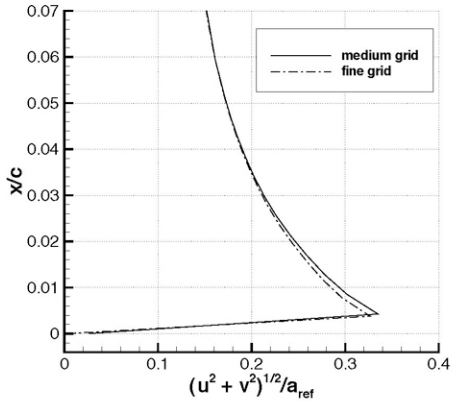

(b) Trailing edge

Mach Contours in Leading and Trailing Edge Regions

$M_\infty = 0.12$, $\alpha = 0°$, $Re_c = 5.45 \times 10^5$, $C_\mu = 0.209$

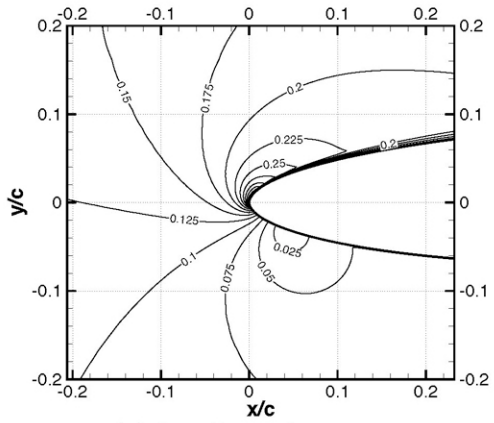

(a) Leading edge

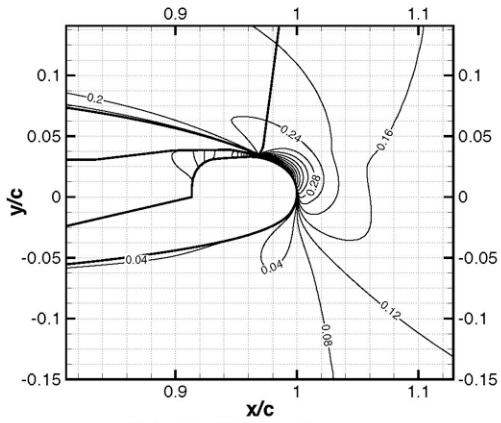

(b) Trailing edge

Mach Contours in Jet Exit Region

$M_\infty = 0.12$, $\alpha = 0°$, $Re_c = 5.45 \times 10^5$, $C_\mu = 0.209$

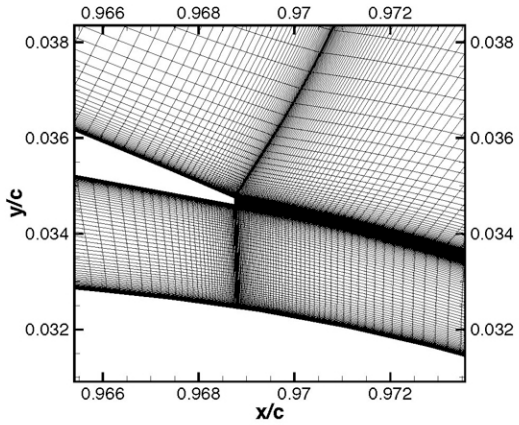

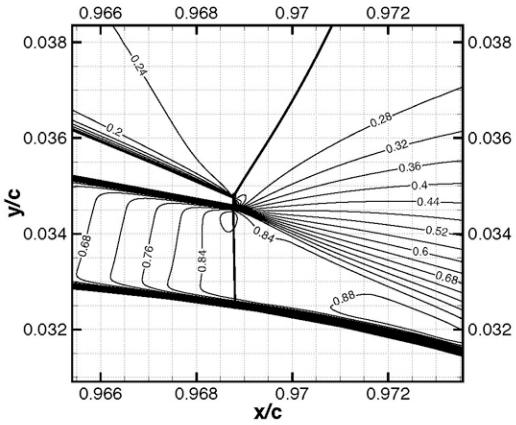

Variation of Lift with Jet Momentum

$M_\infty = 0.12,\ \alpha = 0°,\ Re_c = 5.45 \times 10^5$

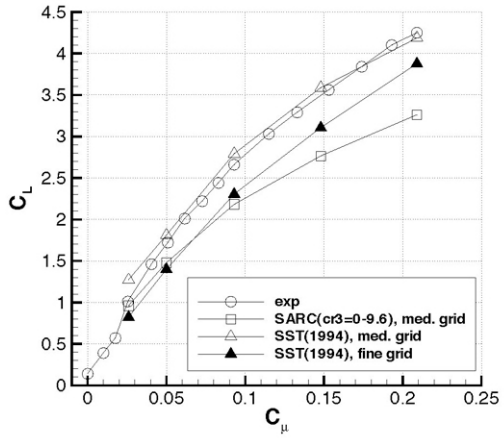

Surface Pressures (Case 321)

$M_\infty = 0.12,\ \alpha = -8°,\ Re_c = 5.45 \times 10^5,\ C_\mu = 0.184$

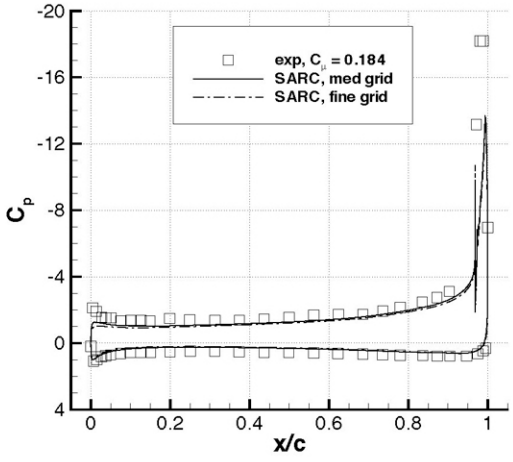

Jet Streamlines (Case 321)

$M_\infty = 0.12$, $\alpha = -8°$, $Re_c = 5.45 \times 10^5$, $C_\mu = 0.184$

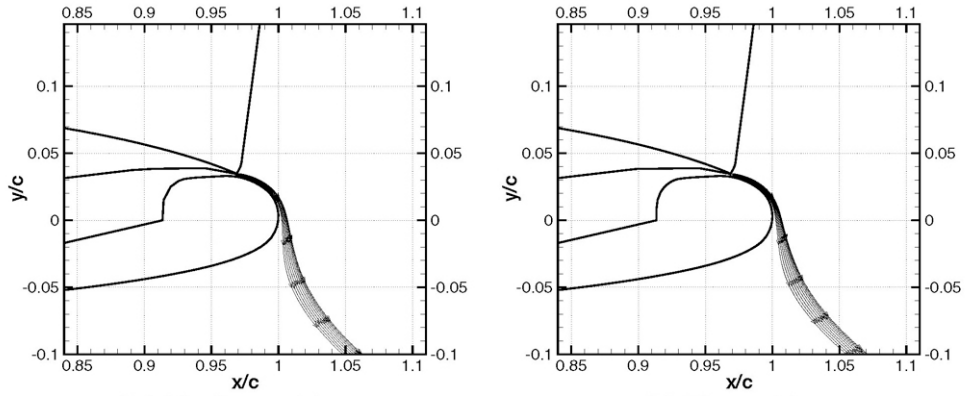

(a) Medium grid (b) Fine grid

Mach Contours in Leading and Trailing Edge Regions

$M_\infty = 0.12$, $\alpha = -8°$, $Re_c = 5.45 \times 10^5$, $C_\mu = 0.184$

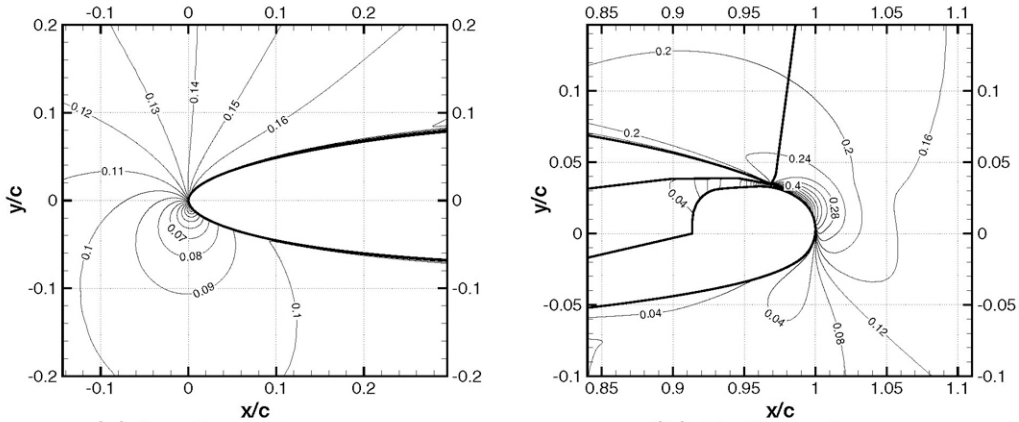

(a) Leading edge (b) Trailing edge

Streamline Pattern at Trailing Edge

$M_\infty = 0.12$, $\alpha = -8°$, $Re_c = 5.45 \times 10^5$, $C_\mu = 0.184$

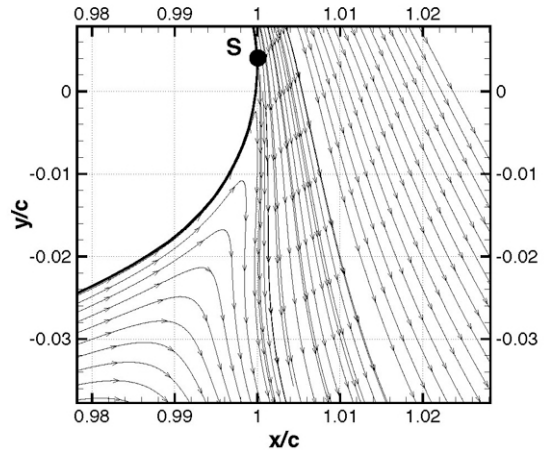

Lift and Drag Coefficients

Case	C_μ	Grid	$(C_l)_{\exp}$	C_l	$(C_d)_{\exp}$	C_d
283	0.209	med.	4.20	3.26	-0.050	0.1140
283	0.209	fine	4.20	3.15	-0.050	0.1090
	0.281	med.		3.62	-0.050	0.1560
	0.342	med.		4.05	-0.050	0.2100
321	0.184	med.	2.40	2.17	-0.080	0.0957
321	0.184	fine	2.40	2.03	-0.080	0.0922

Comparison of computed and experimental lift and drag coefficients for circulation control airfoil.

Conclusions

- Circulation control airfoil flows at different conditions have been considered.
- Various turbulence models based on one and two transport equations have been considered.
- A calibration of the Spalart-Allmaras model with curvature effects (SARC) has resulted in good predictions of pressure distributions.
- Relatively small effects of mesh density have been demonstrated for results with SARC($cr3 = 0 - 9.6$) model.